Genetic relationship among komatiites and associated basalts in the Badampahar greenstone Belt (3.25–3.10 Ga), Singhbhum Craton, Eastern India

Author names and affiliations:

Rupam Ghosh[1], Pieter Vermeesch[2], Debesh Gain[1], Riya Mondal[3]

[1]*Department of Geological Sciences, Jadavpur University, Kolkata, India*

[2]*Department of Earth Sciences, University College London, London, UK*

[3]*Department of Geology, Presidency University, Kolkata, India*

Corresponding author: **Rupam Ghosh**

Email: rupamkumarsp@gmail.com

Abstract

The ultramafic-mafic volcanic rocks of Archean greenstone belts are important archives for lithospheric and asthenospheric processes of the early Earth. Despite decades of research on this context, many issues still remain unsolved. For example, the process of komatiite magma genesis and the genetic relationship among komatiites, komatiitic basalts and tholeiitic basalts in Archean greenstone belts are not clearly understood. The metavolcanic rocks of the Badampahar greenstone belt (BGB), Singhbhum Craton are studied by major-trace element geochemistry to address the said problems and better understand the evolution of melts in Archean lithosphere. Our research suggests that the protoliths of the metavolcanic rocks were komatiites (both Al –depleted and –undepleted), komatiitic basalts and tholeiitic basalts. The Al–heavy rare earth element (HREE) depleted komatiites were formed by moderate degree mantle melting at a higher depth and the Al–HREE undepleted komatiites are products of moderate to high degree mantle melting at a shallower depth. The melting–assimilation–fractional crystallization modelling result shows that komatiitic basalts were generated from Al–undepleted komatiites, and tholeiitic basalts were generated from evolved komatiitic basalts by assimilation and fractional crystallization processes. The older age limit of the BGB is determined to be 3.25 Ga. and the basement of sedimentation and volcanism was composed of plutonic felsic rocks.

Keywords: komatiite; komatiitic basalt; tholeiitic basalt; greenstone belt; crustal assimilation.

1. Introduction

Komatiites together with associated basalts can provide insight into the physicochemical conditions of mantle and magma generation history of the early Earth (Hofmann, 1997; Arndt et al., 2008; Condie, 2015, Condie et al., 2016). Extensive studies have been done on these Archean ultramafic–mafic rocks for the last four decades (e.g., Barnes et al., 1988; Jayananda et al., 2008; Stiegler et al., 2010; Dostal and Mueller, 2013; Konnunaho et al., 2013; Mole et al., 2014; Verma et al., 2017 and references therein). However, many petrogenetic aspects of this rock assemblage still lack transparency. For example, komatiites and komatiitic basalts though have textural–geochemical (major elements) similarities and occur together in greenstone belts, the genetic relationship between them is not clear. It is a matter of debate whether komatiitic basalts were generated by fractional crystallization of komatiites or as primary mantle melt (Arndt et al., 2008 and references therein). A number of studies (e.g. Francis and Hynes, 1979; Arndt and Nesbitt, 1982; and Cattell, 1987) suggest that fractional crystallization and assimilation of komatiites with granitoid rocks might have led to the generation of komatiitic basalts. However, most other studies (e.g. Nesbitt and Sun, 1976; Arndt and Nesbitt, 1984; Arndt et al., 1997; Hanski et al., 2001; Dostal and Mueller, 2013; Verma et al., 2017) consider diverse origins of komatiites and associated basalts. The relationship of tholeiitic basalts with komatiites and komatiitic basalts is also uncertain as tholeiitic basalts have very different and evolved chemical compositions (Arndt, 1991; Condie, 1994). The interlayered association of different volcanic rocks in Archean greenstone belts indicating their formation simultaneously arises questions about their genetic connection. The present paper addresses the aforesaid geological problems with the geochemical evidences gathered from the ‘meta’ ultramafic-mafic volcanic rocks of Badampahar greenstone belt (BGB), Singhbhum Craton, Eastern India.

A number of studies (e.g. Sahu and Mukerjee, 2001; Chaudhuri et al., 2015, 2017) have previously reported presence of ‘meta’ -komatiites and -basalts from the eastern greenstone belts of Singhbhum Craton and the studies were mostly concentrated upon petrogenesis of komatiites. However, none of the studies had attempted to investigate the genetic connection among komatiites and associated basalts of the studied area. Absolute geochronology of the studied greenstone rocks by direct radiometric age dating is absent. Saha (1994) suggested an indirect age ca. 3.3-3.1 Ga of the rocks defined by their stratigraphic relationship with associated granitoid rocks. Hence, a geochronological re-evaluation of the BGB rocks is required alongside the geochemical study of metavolcanic rocks.

The metavolcanic rocks of BGB are studied by major and trace element geochemistry with the following objectives, (i) better understanding the genesis of komatiites, and melt generation processes in Archean mantle, (ii) exploring the genetic connection among komatiites and associated basalts, and (iii) modelling the geochemical evolution of melts in Archean lithospheric reservoirs. We have also studied detrital zircon geochronology of a metaconglomerate (occurring at lower part of stratigraphy) with the objective to know the age and basement rocks of the studied greenstone belt which is relevant to this study.

2. Geological setting

The Singhbhum Craton (Fig.1A) of the Eastern India is bounded by the Singhbhum Mobile Belt to the north, the Bastar Craton to the west, Eastern Ghats mobile belt to the south and southeast (Saha, 1994). It principally comprises Paleo- and Meso- Archean supracrustal rocks belonging to Older Metamorphic Group (OMG), Older Metamorphic Tonalitic Gneiss (OMTG), Singhbhum Granite and equivalents, and Iron Ore Group (Mukhopadhyay, 2001; Table 1). The central part of Singhbhum Craton is principally occupied by granitoid rocks of different generation belonging to Singhbhum Granite, whereas the rocks of other group occur mostly at the peripheral part (Saha, 1994; Mishra et al., 1999). The OMG is the oldest rock group in the craton and it encompasses amphibolite facies supracrustal assemblage of pelitic schists, quartz–magnetite–cummingtonite schists, calc–gneiss and amphibolites (Saha, 1994; Mukhopadhyay, 2001). The depositional time span of OMG rocks is considered between 3.50 Ga. and 3.45 Ga, (U-Pb date of zircon; Goswami et al., 1995; Mishra et al. 1999). A number of studies (e.g. Saha, 1994; Gowshami et al., 1995; Upadhyay et al., 2014) reported that the OMG rocks occur as enclaves within younger tonalities-trondhjemites-granodiorites (TTGs) belonging to OMTG. The first phase of the TTGs was emplaced around 3.45 Ga (U-Pb date of zircon; Mishra et al., 1999; Acharyya et al., 2010; and Upadhyay et al., 2014). Upadhyay et al. (2014) reported another younger phase of it emplaced around 3.32 Ga (U-Pb date of zircon). The OMG and OMTG occur as enclave within Singhbhum Granite, and the biggest exposure of them is located at the western part of the craton (Fig. 1B), near village Champua (Mukhopadhyay, 2001). The Singhbhum Granite mainly comprises granodiorites, trondhjemites and granites (Saha, 1994). Upadhyay et al. (2014) reported that three major phases of Singhbhm Granite Type–A plutonic intrusions occurred synchronously with OMTG emplacement during 3.44 Ga, 3.35 Ga and 3.32 Ga (U-Pb date of zircon). The plutonic intrusions of Singhbhm Granite Type–B (ca. 3.12 Ga; Pb-Pb date by Ghosh et al. 1996) and equivalent rocks such as Bonai granite (ca. 3.16 Ga; U-Pb date of zircon by Sengupta et al., 1996) and Mayurbhanj granite (ca. 3.09 Ga; U-Pb date of zircon by Mishra et al., 1999) happened after deposition and metamorphism of the Iron Ore Group rocks (Saha, 1994).

At the peripheral part, the Singhbhum Craton is flanked by several greenstone belt successions (belonging to the Iron Ore Group) which are exposed near the Jamda–Koira region in the west, the Gorumahisani–Badampahar region in the east and the Tomka–Daitari region in the south. Saha (1994) interpreted them to be formed in between 3.3 Ga and 3.1 Ga by their stratigraphic relationship with associated granitoid rocks. The volcano-sedimentary greenstone sequences are mostly consisting of banded iron formations, mafic-felsic volcanic rocks, shale, quartzite, chert and carbonates (Saha 1994; Mukhopadhyay, 2001). The Badampahar greenstone belt (BGB) occurs at the southern part of the Gorumahishani–Badampahar region (eastern Iron Ore Group; Fig. 1B). The rocks of the BGB are metamorphosed from greenschist to lower amphibolite facies (Saha, 1994; Ghosh and Baidya, 2017a).

3. Stratigraphy and sampling

The BGB majorly comprises interbedded sequence of metavolcanic rocks, quartzite, banded iron formations, chert and phyllite along with minor metavolcaniclastics and schists (Fig. 1C). Detailed structural study reveals at least four major phases of deformation (Ghosh and Baidya, 2017a). The first deformation phase (D_1) developed the regional Badampahar isoclinal fold (F_1) plunging 63^0 towards NNE and foliation S_1. The second deformation (D_2) caused extensive shearing and folding (F_2) with the development of S_2 foliation. S_2 dips from 75^0 to 85^0 towards NW. Isoclinal to tight F_2 folds plunge from 25^0 to 63^0 towards NE or SW (Fig.1C: near Jashipur). The third deformation phase (D_3) caused open type folds (F_3) plunging from 40^0 to 75^0 towards NW. Faults and joints were developed subsequently. Three sets of fault trending NW-SE, E-W and N-S are interpreted from field and satellite imagery. Three sets of penetrative joints are present, dipping 80^0 - 85^0 towards ESE, 70^0 - 80^0 towards SE to SSE and vertical joints trending N-S.

Stratigraphic sections were prepared based on mapping along AB, CD, EF, GH, IJ, KM, LM, OP and NP on the limbs of regional isoclinal fold (Fig. 1C). Cross stratification and normal graded bedding in quartzites and pillows in metavolcanic rocks confirmed the local younging direction of the sequences, and, together with the broad F_1 and F_2 fold structure, allowed regional correlations. The stratigraphic sections are thoroughly described in Supplementary material 1. In summary, most stratigraphic sections of the BGB show that the lower and upper –part of the sequences (Fig. A1, A3 and A5, Supplementary material 1) are occupied by metavolcanic rocks (Fig. A2a-A2e, supplementary material 1) along with a few sedimentary interbeddings. Section EF and GH exceptionally do not comprise a lower and an upper metavolcanic rock horizons. The middle part of all stratigraphic sections are mostly occupied by sedimentary rocks. The metavolcanic rock horizons of the middle part are relatively thin (10–20 m) and interlayered with sedimentary rocks (Fig. A2f, supplementary material 1). Correlation of the stratigraphic sections in the BGB led to categorise the metavolcanic rocks in three groups, namely basal–, middle– and upper– metavolcanic rocks.

A total twenty three fresh metavolcanic rock samples devoid of any vesicle/amygdule, visible weathering and hydrothermal vein are selected for bulk geochemical analyses. Among them, eleven samples of the basal–metavolcanic rocks from section AB, NP and KM, six samples of the middle–metavolcanic rocks from section EF and GH, six samples of the upper–metavolcanic rocks from section AB, LM and IJ are selected for analysis (Supplementary material 1). We collected the metaconglomerate sample (A33) from section IJ for petrography and detrital zircon dating.

4. Analytical techniques

Electron probe micro analyser (EPMA) was used to determine the chemical compositions of minerals present in the studied metavolcanic rocks. EPM analysis was done using a ‘CAMECA SX Five’ model in the laboratory of Indian School of Mines, Dhanbad, India with an accelerating voltage 15kV, current 12nA and 1 μm beam diameter. Standards were run before and after analysis to determine the analytical error. The analytical inaccuracies and uncertainties of the analysis are negligible and as follows: <0.1% for Cr; <1% for P, Al, Si, K, Ca, Fe, Mg, Ti, V; <2% for Mn and Na.

The metavolcanic rock samples were pulverized for major, trace and rare earth elements (REEs) analyses at the laboratory of Australian Laboratory Services Pty Ltd., Perth, Australia. The samples were digested and analysed for major oxides in inductively coupled plasma–atomic emission spectroscopy (ICP–AES) following the methods of Murray et al. (2000). For trace and REEs, the samples were acid digested and analysed using inductively coupled plasma–mass spectroscopy (ICP–MS) following the methods of Qing et al. (2003). The laboratory standard reference materials namely OREAS146, GGC–8, GGC–10, GBM908–10 and MRGEO08 are analysed along with each batch for accuracy and precision. The analytical uncertainties for major and trace elements are <4% and <10%. The complete dataset with sample location is available in Table A3 (Supplementary material 5).

Zircon grains were separated from the metaconglomerate by conventional magnetic and heavy liquid separation after crushing and grinding. The separated zircon grains were mounted in Araldite on glass slides and polished. The U–Th–Pb isotopic analyses were done on an Agilent 7700x ICP–MS coupled to a NWR193 excimer laser system at the London Geochronology Centre. Zircons were dated ‘blindly’ so as to avoid selection bias (Garzanti et al., 2018), and were only subjected to cathodo–luminescence imaging after U–Pb analysis. The laser was operated at 20Hz pulse repetition rate, >2 J/cm2 energy density, 25 µm laser pit diameter and 20s duration. Plešovice zircon and NIST SRM612 glass were analysed along with the studied zircons for age and concentration standardization. Linear fit through the standards yielded a fit within 1% for the $^{206}Pb/^{238}U$ ratios. Data reduction was performed using Glitter 4.4 (Griffin et al., 2008). The complete dataset with sample location is available in Table A2 (Supplementary material 4). Further post processing, including concordia analysis and kernel density estimation were done with IsoplotR version 1.1 (Vermeesch, 2018).

5. Detrital zircon geochronology of metaconglomerate

The metaconglomerate horizon in stratigraphic section IJ (250m) overlies a quartzite horizon and grades upward to another quartzite (Fig. A5; Supplementary material 1). The metaconglomerate is clast supported with minor quartz rich matrix (< 10 modal %). Secondary chloride–sericite–goethite are present along the clast boundaries and inter–granular spaces (Fig. 2A, 2B). The clasts are well rounded and ellipsoidal with 1–2 cm long axes. The long axes of the clasts are oriented along the regional first generation foliation plane (S_1) corresponding to D_1/F_1 (Fig. 2A). The clasts consist mostly of quartz aggregates with minor K–feldspar, zircon and apatite. The quartz grains exhibit a crude interlocking texture with mostly straight and sharp grain boundaries (Fig. 2B, 2C and 2D). However, some grain boundaries are weakly diffused by pressure solution. The zircon grains of various size (20–200μm long axis) and shapes are present as inclusion within quartz.

The CL images of the analysed zircon grains exhibit distinct oscillatory growth zoning by alternating high and low CL response to the zones (Fig. 2E–2L). Plotting the U–Pb data for sample A33 on a Wetherill concordia diagram (Fig. 3A, 3B) defines a discordia trend with a ∼875 Ma lower intercept which indicates partial Pb–loss during an unidentified Neoproterozoic tectonic event. The Kernel Density Estimate (KDE, Vermeesch, 2012) of the concordant ages reveal two distinct components at ∼3.30 and ∼3.45 Ga., respectively (Fig. 3C). The age of the youngest zircon grain of the assemblage is 3.25 Ga.

6. Petrography and geochemistry of the metavolcanic rocks

6.1. Petrography

The rocks of BGB have endured multiple events of deformation and metamorphism. Hence, original igneous texture is almost obscured and initial minerals are replaced by secondary metamorphic minerals. However, the rocks could be classified into three groups based on metamorphic mineralogy and texture. The first group of rocks primarily consists high-Mg silicate minerals such as serpentine and talc (65-80 modal %) with the ubiquitous presence of tremolite (10-15 modal %) and magnetite (15-20%). Secondary minerals such as serpentine, talc and tremolite pseudomorph after original igneous minerals (e.g. olivine, orthopyroxene and clinopyroxenes) in these rocks (Fig. 4A and 4B). The coarse (200-1000µm) pseudomorphic- and magnetite- crystals occur within the fine (20-100µm) serpentine-talc rich groundmass (Fig. 4A and 4B). Olivine and pyroxenes are absent in these rocks due to their complete alteration to secondary minerals. Relict of spinifex texture can be identified in some samples by radiating long (3-5 mm) skeletal/acicular crystals of magnetite and talc-serpentine pseudomorphs after olivine/orthopyroxene (Fig. 4C). The second group of rocks consists tremolite-actinolite (50-70 modal %), magnetite (10-15 modal %) and serpentine-talc (20-30 modal %) as major minerals and plagioclase (<2-10 modal %) as minor mineral (Fig.4C and 4D). Whereas, the third group of rocks are primarily consist of hornblende (65-85 modal %) and plagioclase (10-25 modal %) and magnetite (5-10 modal %) (Fig. 4E and 4F). Ilmenite, titanite, zircon, apatite and sulphides are present as accessory minerals in these rocks. The amphibole porphyroblasts varies in size from very fine (100µm) to coarse (2000µm) crystals. Most samples show strong metamorphic fabric defined by amphibole grain alignment along regional first generation foliation plane (Fig. 4E and A2d, supplementary material 1). Post-kinematic amphibole porphyroblasts cut across this fabric. Original igneous minerals and textures are though absent, some of the rocks contain initial ophitic and subophitic textural outlines preserved in aggregates of plagioclase and amphibole crystals (Fig. 4D and 4F). The amphiboles are possibly pseudomorphs after clinopyroxene. The plagioclase crystal varies in compositions (albite-andesine) and in size (from 100µm to 1000µm) both within sample and between samples.

6.2. Effect of metamorphic and post–metamorphic events

The rocks of BGB have experienced multiple phases of deformation, up to lower amphibolite facies of metamorphism and some hydrothermal events (Ghosh and Baidya, 2017a) which may mask the original geochemical characteristics. Therefore, it is important to detect those altered rocks by petrography and geochemical filters before any interpretation. The analysed rocks are examined under microscope, and most of the samples are free from any visible alteration, amygdule/vesicle and hydrothermal veins. The loss in ignition (LOI) values indicate presence of volatiles in rock (as carbonate minerals) and may indicate degree of alteration. Most of the studied rocks have low LOI content ranging from 0.79 to 2.25 wt. %, but some of them (sample E35, D84, D79, E32, E24, D118 and D120) have little higher LOI values ranging from 4.79 to 10.68 wt. %. However, the carbon concentration (<0.1 wt. %) is negligible in all of the samples (Table A3, supplementary material 5). This rules out the possibility of element incorporation from external source by carbonate alteration. The high LOI values are due to the hydrous silicate mineralogy (e.g., hornblende, talc and serpentine) of the studied rocks. Moreover, the LOI values show little or no correlation with Nb/La and Th/La ratios (as La is considered less mobile in alteration relative to Nb and Th) indicating that the elemental ratios have not been affected by the increase of volatile content (Fig. A6, Supplementary material 3). Zirconium is one of the least mobile elements and it may be used as a reference to test the mobility of other elements. The Zr vs. major oxides (Fe_2O_3, MgO and TiO_2), high field strength elements (HFSEs; Th and Nb) and REEs (La, Sm and Yb) diagrams (Fig. A7 and A8, Supplementary material 3) show mostly coherent trend or limited scatter (exception for sample D79), implying immobility of the elements during metamorphic and post–metamorphic events. The NMORB (Sun and McDonough, 1989) normalized multi–element spider diagram (Fig. A9, supplementary material 3) shows sub–parallel/parallel REE and HFSE (Hf, Zr, Ti, Ta and Nb) patterns of the metavolcanic rocks (exception for D79) indicating minor or no mobility during metamorphism. This fact is also supported by near zero Ce_{CI} and Eu_{CI} (CI chondrite normalized) anomalies of the most analysed samples (Table 3) as considerable amounts of Ce and Eu anomalies indicate alteration by weathering and hydrothermal processes. The LILE are considered highly mobile elements during metamorphism and alteration. Most of the metavolcanic rock samples show irregular and enriched LILE patterns which are expected in deformed–metamorphosed Archean greenstone rocks. The metavolcanic rock samples excluding sample D79 are considered for geochemistry and mainly the less mobile elements such as transition metals, HFSEs and REEs are selected for interpretation.

6.3. Major and trace element compositions

The metavolcanic rocks are characterized by variable but significant contents of SiO2 (38.4-57.4 wt. %), Al_2O_3 (1.41–13.15 wt. %), CaO (1.52–11.9 wt. %), $Fe_2O_3^T$ (8.47–17.3 wt. %), TiO_2 (0.07–1.91 wt. %) and MgO (3.05–32.7 wt. %) and Mg# varies between 15 and 75 (Table A3, Supplementary material 5). They dominantly occupy the area of basalt to basaltic andesite protolith in SiO_2 vs. K_2O+Na_2O plot (TAS; after Le Bas et al., 1986; Fig. 5A) and Nb/Y vs. Zr/Ti plot (after Pearce, 1996; Fig. 5B). The subalkaline nature of these rocks are also evident in the TAS diagram due to their low alkali element concentrations (Irvine and Baragar, 1971).

The metavolcanic rocks based on MgO contents (and petrographic study) can be divided into three groups those will be later determined to be komatiites, komatiitic basalts and tholeiitic basalts. Group–I rocks (Sample E35, D84, E32, E25, E24, D118 and D120) have MgO values between 19.05 and 32.7 wt. %; group–II rocks (Sample E34, E39, E36, E37, E40, E44, D11, E38, A10, E23, D123 and A26) have MgO values between 8.47 and 14.55 wt. %; and group–III rocks (Sample D33, E11, E13, E17, E22 and D111) have MgO values between 3.05 and 6.46 wt. %. These groups also have contrasting SiO_2, Al_2O_3, Ga, Ni, Cr, Co, Y and Zr concentrations. For example, the group–I rocks contain lower concentrations of SiO_2 (38.4–48.4 wt. %), Al_2O_3 (1.41–8.01 wt.%), Y (2.7–7.9 ppm), Ga (1.5–6.5 ppm), V (24–163 ppm) and ∑REE (3.1–33.98 ppm) and higher concentrations of Cr (960–6410 ppm), Ni (777–2340 ppm) and Co (75–125 ppm) than the group–II and group–III rocks. Concentrations of Al_2O_3 (5.73–10.95 wt.%), Y (9.4–17.9 ppm), Ga (8.1–12.2 ppm), V (159–279 ppm), Cr (600–1490 ppm), Ni (173–525 ppm), Co (50–77 ppm) and ∑REE (14.28–44.27 ppm) in the group–II rocks are intermediate relative to other groups. The group–III rocks have higher concentrations of Al_2O_3 (10.4–13.15 wt.%), Y (16.8–45.9 ppm), Ga (16.4–19.1 ppm), V (243–454 ppm) and ∑REE (50.12–134.9 ppm) and lower concentrations of Cr (40–380 ppm), Ni (51–114 ppm) and Co (40–51 ppm) than the group–I and group–II rocks (Table A3, Supplementary material 5). The group–I and group–II rocks also have lower Zr and Nb concentrations (Zr~6–64 ppm and Nb~ 0.2–3.4 ppm) than group–III rocks (Zr~84–239 ppm and Nb~4.6–12.4 ppm).

The group–I metavolcanic rocks have MgO >18 wt. % which may be present in few high Mg volcanic rocks such as, komatiites, picrites, meimechites and boninites. Among them, meimechites and komatiites have Na_2O+K_2O values (<2 wt. %) less than picrites (Maitre et al., 1989). Meimechites have generally high TiO_2 contents (>1 wt. %) and boninites have high SiO_2 contents (>53 wt. %) which are absent in komatiites (Le Bas, 2000). Boninites also show high LILE concentrations and ‘U’ shaped chondrite normalized REE patterns due to MREE depletion (Smithies et al., 2004). The Group–I rocks have Na_2O+K_2O contents between 0.06 and 0.56 wt. % (Fig. 5A), TiO_2 values between 0.07 and 0.65 wt. %, SiO_2 values between 38.4 and 48.4 wt. % and low LILE contents (Table A3, Supplementary material 5). These also do not exhibit depleted MREE patterns in chondrite normalization (Fig. A9 in supplementary material 3; Table 3). Therefore, protolith of group–I metavolcanic rocks was komatiite. These also occupy the komatiite zone in the Mg–Fe+Ti–Al triangular diagram proposed by Jensen (1976), along with group–II rocks at the komatiitic basalt zone and group–III rocks at high Fe tholeiite zone. In MgO vs. TiO_2 diagram (after Arndt et al., 2008), group–I rocks are also plotted at the komatiite zone (Fig. 5D). These have Mg# between 59 and 75, Al_2O_3/TiO_2 ratios between 2.43 and 61.6, and CaO/Al_2O_3 ratios between 0.37 and 4.2 (Table 3).

Komatiitic basalts are generally distinguished from other basalts by their spatial association with komatiites, textures and chemical compositions. For example, these have lower MgO values (between 18 and 6 wt. %) and higher Al_2O_3, Ti and Zr values than komatiites and they plot at the extension of chemical trends defined by komatiites (Arndt et al., 1977; Arndt and Nebitt, 1982; Arndt et al., 2008). The group–II rocks are interbedded with the komatiites (group-I rocks) in the BGB volcano–sedimentary sequences and have lower MgO and higher Al_2O_3 values than komatiites. These also have low TiO_2 (<1 wt. %) and Zr (<64 ppm) values similar to komatiites (Table A3, Supplementary material 5) and occur at the extension of chemical trends of komatiites (Fig. 6). Therefore, the protolith of group–II metavolcanic rocks was komatiitic basalt.

The group–III rocks have higher $Fe_2O_3^T$ and lower MgO concentrations (Mg#<40) than group–II komatiitic basalts (Table 3). These also contain higher concentrations of Al_2O_3, HFSEs (TiO_2~0.86-1.91 wt. %; Zr~84–239 ppm and Nb~4.6–12.4 ppm) and REEs relative to the first two groups (Table A3, Supplementary material 5) and plot at the high Fe tholeiitic basalt zone in Mg–Fe+Ti–Al triangular diagram (Fig. 5C; after Jensen, 1976).

The trace element$_{CI}$ patterns (CI chondrite normalized) of komatiites, komatiitic basalts and tholeiitic basalts in multi–element spider diagram (Fig. A11, supplementary material 3) shows that all elements are enriched (>1) relative to the CI chondrite values. The patterns are characterized by overall enrichment of LREE$_{CI}$ relative to HREE$_{CI}$ and Ba, Rb, Th and U relative to other elements. While most komatiites have depleted HREE$_{CI}$ (Gd/Yb $_{CI}$ ~ 1.38–2.68) relative to LREE$_{CI}$ and MREE$_{CI}$, some komatiites (E24 and E35) are also enriched in HREE$_{CI}$ (Gd/Yb $_{CI}$ ~ 0.453–0.632) (Table 3). Komatiitic basalts are overall enriched in LREE$_{CI}$ and MREE$_{CI}$ (La/Yb $_{CI}$ ~ 1.09–4.04; Gd/Yb $_{CI}$ ~ 1.06–1.97) relative to HREE$_{CI}$ (exception for sample E34 and A10 having depleted LREE$_{CI}$; La/Yb $_{CI}$ ~ 0.669–0.784). Tholeiitic basalts have also enriched LREE$_{CI}$ and MREE$_{CI}$ (La/Yb $_{CI}$ ~ 2.30–5.98; Gd/Yb $_{CI}$ ~ 1.19–1.60) relative to HREE$_{CI}$ (Table 3).

7. Discussion

7.1. Basement and age of the BGB rocks

The consisting minerals of metaconglomerate clasts have retained their primary igneous textures even after multiphase deformation and metamorphism. The mineralogy (quartz with minor K–feldspar, apatite and zircon) and igneous texture of the clasts indicate that they were derived from felsic plutonic igneous rocks dated before the BGB rocks. The analysed zircon grains present in the clasts show igneous oscillatory growth zoning (Fig. 2E-2L) as well as U/Th ratios between 0.33 and 1.56 (Table 2) indicating their igneous origin (Mass et al., 1992). The U–Pb ages of the zircons range from 3.51 Ga. to 3.25 Ga. with two major peaks around 3.45 Ga. and 3.30 Ga. indicating two major source of the zircons. The older peak matches well with the OMTG rocks and the younger peak matches with the OMTG granite and third phase of SBG Type–A (Table 1). This implies that the TTGs and granites of OMTG and granites of third phase SBG Type–A were the exposed rocks during the deposition of BGB sediments and volcanics. They acted as the basement for BGB, supplied sediments and possibly contaminated the volcanic rocks. The youngest zircon of the suite is aged 3.25 Ga. which is the maximum depositional age of the BGB metaconglomerate.

The metaconglomerate horizon is one of the basal unit of BGB stratigraphy (Fig. A5c, supplementary material 1). This implies that the older age limit of the BGB rocks is 3.25 Ga. which is 50 Ma. younger than the previously reported older age limit by Saha (1994). Hence, the more precise geological time span of BGB rocks is between 3.25 Ga. and 3.1 Ga.

7.2. Petrogenesis of the BGB metavolcanic rocks

The metamorphosed volcanic rocks of the BGB are mostly massive to amygduler/vesicular and occasionally have intact pillow structures (Fig. A2, supplementary material 1). The presence of pillows as well as intercalated sedimentary rocks (e.g. BIF) clearly indicate a submarine depositional setting. Metamorphism and deformation have obscured original mineralogy and textures. However, they can be classified into komatiites, komatiitic basalts and tholeiitic basalts based on their geochemical characteristics.

There are two types of komatiites present in the BGB, Al–depleted (D84, E32, E25, D118and D120 having Al_2O_3/TiO_2 ratios between 2.43 and 18.54) and Al–undepleted (E35 and E24 having Al_2O_3/TiO_2 ratios around 61.6). The Al–depleted komatiites have depleted $HREE_{CI}$ (Gd/Yb $_{CI}$ ~1.20–2.68), whereas, Al–undepleted komatiites have enriched $HREE_{CI}$ (Gd/Yb $_{CI}$ ~ 0.45–0.63; Table 3). When melt is produced by moderate degree mantle melting at a higher depth (>9 GPa.), ferromagnesian minerals like olivine and orthopyroxene are melted while garnet being stable at high pressure remains in residual solid. Melting in this way is responsible for the formation of Al– and $HREE_{CI}$– depleted komatiites. Besides, when higher degree melting of mantle takes place at relatively shallower depth (<7 GPa.), garnet is melted along with olivine and orthopyroxene, and the magma is enriched in Mg as well as undepleted in Al and $HREE_{CI}$ (Green, 1975; Sun and Nesbitt, 1978; Herzberg and Ohtani, 1988; Hetzberg, 1992).

The intercalated volcanic flows of different compositions occur all over the stratigraphic columns of the BGB without any distinct consecutive order (Supplementary material 1). For example, komatiite (sample D120) and komatiitic basalt (sample D123) flows occur at upper stratigraphic position of tholeiitic basalt (sample D33) flows in section AB (Fig. A1, supplementary material 1), whereas, the basal part of the section is occupied by pillows of komatiitic basalt (sample A10). The basal volcanic part of section KM is dominated by tholeiitic basalt flows (Fig. A3, supplementary material 1), whereas, basal part of section NP is majorly occupied by komatiitic basalt flows (Fig. A5, supplementary material 1). This type of situation is not uncommon in other Archean greenstone successions. For example, Cattell (1987) reported intercalated sequences of komatiites and komatiitic basalts bounded by tholeiitic basalts in some parts of Abitibi greenstone belt, Canada. Such episodic change of erupting magma composition may indicate two major possibilities, 1) generation of different magmas from different sources and 2) different degree of partial melting of a source accompanied by variable degree of fractional crystallization, assimilation and mixing.

The studied rocks form continuous data arrays in different binary geochemical plots of elements such as compatible vs. incompatible, compatible vs. compatible (Fig. 6) and incompatible vs. incompatible (Fig. 7 and Fig. A10, supplementary material 3). The komatiitic basalts followed by tholeiitic basalts plot at the extension of chemical trends defined by komatiites. The continuous projection of the rock compositions in binary diagrams indicate an apparent genetic link of the corresponding melts and eliminate the possibility of different magmatic sources for these rocks. The incompatible (Al, V, Zr, Th, Sm, Nb, Y and Yb)- and compatible (Mg, Cr and Ni)- elements exhibit respective rise and fall in abundance along with the melt evolution from komatiitic to tholeiitic. Interestingly, the compositions mostly follow curvilinear paths (projection of best fit polynomial trend) in the binary diagrams (Fig. 6 and 7; Fig. A10 in supplementary material 3). The slope of most trend lines becomes steeper (for MgO vs. incompatible elements, and Sm vs. Th) or gentler (for MgO vs. Ni, Zr vs. Y and Yb, and Th vs. Yb) for komatiitic- and tholeiitic- basalts. During the formation of basalts, the concentration changing rate of some elements in melt was higher relative to the others (e.g., Ni, V, Al and Zr relative to MgO; Zr relative to Y and Yb, and Th relative to Sm and Yb), and this resulted such curvilinear projections of trend lines. The trend line slope for komatiites is negative in MgO vs. CaO and Sc diagrams and it turns positive for basalts. This indicates different nature of concentration changing of these elements during komatiites and basalts formation. Such change of elemental ratios in binary diagrams can be correlated with the melt evolution processes including fractional crystallization and crustal contamination in the following section.

7.2.1. Role of fractional crystallization and crustal contamination in melt chemistry

The positive correlation of Cr and Ni with MgO defines simultaneous elimination of MgO, Cr and Ni from initial melt by fractional crystallization. The chemical trend of MgO with Cr is linear, but the trend slope with Ni becomes gentler for komatiitic– and tholeiitic– basalts (Fig. 6). The MgO rich early crystallizing minerals, usually, olivine and orthopyroxene have high partitioning coefficient values for Ni which result in rapid depletion of Ni in melt (Arndt et al., 2008). However, Cr does not partition into olivine, rather positive correlation of Cr with MgO may only be generated by chromite crystallization alongside olivine (Barnes, 2000). The relationship of CaO and MgO partitioning from melt was negative during komatiite formation and positive during komatiitic– and tholeiitic– basalt formation. This indicates that CaO was not removed from parental melt during the formation of komatiites and minor/no crystallization of CaO rich minerals occurred alongside MgO rich minerals. However, during the formation of komatiitic– and tholeiitic– basalt, CaO was partitioned from original melt together with MgO. This may define fractional crystallization controlled by CaO–MgO rich minerals (usually clinopyroxene) and CaO rich minerals (usually plagioclase) along with MgO rich minerals (olivine and orthopyroxene). But, unlike CaO, Al_2O_3 shows negative trend with MgO for komatiitic– and tholeiitic– basalts which rules out the possibility of plagioclase fractionation and its control on melt compositions. The fractionation behaviour of Sc (which is highly compatible in clinopyroxene relative to others) similar to CaO also supports this event. The negative correlation of SiO_2, Al_2O_3, V, Zr, Nb and Yb with MgO indicates progressive increase of SiO_2, Al_2O_3, V, Zr and Yb values and depletion of MgO in melt due to incompatibility of these elements in early crystallizing MgO rich minerals e.g olivine and pyroxenes. The trend slopes for HFSEs become steeper for komatiitic– and tholeiitic– basalts indicating rapid increase of those elements in melt with the decrease of MgO concentrations. This is apparently unexpected as the partitioning coefficient values of HFSEs are higher (though not significantly) in clinopyroxene relative to olivine and orthopyroxene (GERM database) which should had caused an opposite situation. This may indicate either rapid crystal growth of minerals in komatiites leading to disequilibrium trace elemental partitioning or increase of HFSEs concentration in evolved melts by crustal contamination accompanied by fractional crystallization. However, significant disequilibrium trace element partitioning in minerals of komatiites would cause scattered plot of the trace elements which is mostly absent (exception for Cr) in the binary diagrams (Fig. 6).

By definition, incompatible elements (having low partitioning coefficients for early crystallizing minerals, GERM database) do not participate significantly in fractional crystallization processes. Their abundance in melt though increases with fractional crystallization, the elemental ratios remain unaffected. Therefore, mantle generated melt that is not contaminated with crustal components would exhibit the incompatible elemental patterns equivalent to that of mantle. Zirconium and Th are highly enriched in continental crust relative to Sm, Y and Yb (Taylor and McLennan, 1985). Contamination with continental crust would result in increase of Th/Yb, Th/Sm, Zr/Y and Zr/Yb ratios. Most studied rock samples exhibit the said ratios higher than mantle ratios (Fig. 7) indicating their contamination with crustal components. Such assimilation with crustal components might had happened directly, by thermal erosion of crustal rocks within crustal chambers, magma tube and at surface, or indirectly, by mixing of melt with crustal component rich continental lithospheric mantle, or all of the processes together. To understand the crust vs. mantle contamination process, we plotted the studied rock compositions in La/Sm vs. La/Ta binary diagram (Fig. 8) after Lassiter and DePaolo (1997). Most of the komatiites and basalts of the BGB follow trend parallel to crustal contamination line in the diagram and therefore indicate the possibility of their direct assimilation with crustal material.

7.2.2. Modelling of melting, fractional crystallization and crustal contamination

To understand the melting and assimilation–fractional crystallization (AFC) process responsible for different melt composition in the studied area, we used "PETROMODELER" excel spreadsheet (Ersoy, 2013). We have tried to address the possible ways of changing magmatic compositions using Zr/Y vs. Yb AFC modelling (Fig. 9). For melting modelling, we used primitive mantle (PM) data of Palme and O'Neill (2014) as melt source composition (C_o^M). For assimilation–fractional crystallization modelling, we have used data of granodiorite (3.3 Ga; Nelson et al., 2014) occurring nearby the BGB as a possible contaminant (C_a). Partitioning coefficient data of Yb, Zr and Y used for fractional crystallization modelling are taken from GERM database. The results of the melting and AFC modelling are as follows.

The Al–depleted komatiite compositions could be generated by 25% garnet–lherzolite facies melting (Walter, 1998) of PM and followed by AFC~ 18–36% and r (ratio of assimilation rate and fractional crystallization rate) ~ 0.27 (Fig. 9A). The Al–undepleted komatiite compositions (e.g. E35 and E24) could be formed by different degree spinel–lherzolite facies melting (Kinzler, 1997) of PM. The E35 composition was possibly formed by 29% melting followed by AFC ~ 18% with r= 0.27, whereas, E24 was formed by 23% melting followed by AFC~ 12% with r=0.27 (Fig. 9B). The komatiitic basalts could not be generated from the Al depleted komatiites or Al–undepleted E35 by AFC. The melt compositions generated from these komatiites do not reach the komatiitic basalt compositions successfully and only the E24 melt composition is suitable for being the parental melt composition. The reason is that E24 has the lowest incompatible element contents as well as it exhibits incompatible elemental ratios same as mantle (Fig. 7). Eventually, Al-undepleted E24 komatiite was the least fractionated and contaminated melt (most primitive) composition among other komatiites. Therefore, the komatiitic basalts could be the products of Al–undepleted E24 komatiite melt or similar melt compositions formed by moderate degree melting of mantle.

Most komatiitic basalts (exception for E38 and E39) could be generated by AFC of E24, where AFC varied from 18 to 50 % and the r value was between 0.10 and 0.28 (Fig. 9C). The more evolved komatiitic basalt compositions, like E38 and E39 could be reached by AFC of other more primitive komatiitic basalt compositions such as E34. The E38 and E39 compositions could be formed by AFC ~30% and r=0.23 of E34. The tholeiitic basalts were generated by AFC of various komatiitic basalt compositions. For example, the D33 melt composition was the result of AFC ~18% with r=0.27 of D123. The D111 was formed by AFC~ 50% with r=0.27 of E38. The E17, E13 and E11 was formed by 54% fractional crystallization without significant assimilation of E38 melt composition. The most evolved tholeiitic basalt E22 could be formed by AFC~30% with r=0.59 of E17 or similar melt compositions (Fig. 9D).

To verify the AFC model, we tested the melt composition evolution on multi-element (HFSEs and REEs) spider-diagram (Fig. 10). We selected some melt compositions those represents each melt groups e.g., Al-undepleted komatiite (E24, starting composition), primitive komatiitic basalt (E34), evolved komatiitic basalt (E38) and tholeiitic basalt (D111). The E34 composition could be successfully reached by AFC ~ 45% (r=0.14) of E24 similar to the previous modelling results. The composition E34 could be evolved to E38 by AFC~ 36% (r=0.35) and composition E38 could be evolved to D111 by AFC~ 45% (r=0.27). The multi-element AFC results match well with the previously determined bi-variant AFC results.

In summary (Fig.11), the more primitive melt compositions (komatiitic) were episodically introduced into the magma chambers of the studied greenstone belt and were evolved by fractional crystallization and assimilation. The komatiite melts were generated at different depth of mantle with different melting degrees, possibly from rapidly ascending mantle plume. As stated in the introduction section, the genetic relationship of komatiites, komatiitic basalts and tholeiitic basalts are highly debated instead of their close field association. Nesbitt and Sun (1976) and Arndt and Nesbitt (1984) proposed that the basalts were formed by low–moderate degree melting of different parts of the mantle source that produced komatiites. Campbell et al. (1989) proposed that komatiites were originated from hot axis of mantle plume and the other basalts are melting product of cooler plume annulus. However, our study suggests that the komatiitic basalts could be generated by AFC of Al–undepleted komatiites (e.g. E24) formed by moderate degree melting at relatively lower pressure. It was also noted that the tholeiitic basalts could not be formed by even 90% AFC of a komatiite melt, but, they could be formed by AFC of evolved komatiitic basalt melts. However, it is difficult to imagine that a melt composition (e.g. E38) generated by 30% AFC, again participated in 50–54% AFC to form another melt (e.g. D111 or E17). This is possible only if the residual melt of evolved komatiitic basalt composition was separated out in a different magma chamber and went through another AFC process.

The komatiite-basalt succession of the BGB, Singhbhum Craton may be geologically compared with similar type Archean volcanic successions present in Stoughton-Rouemature group (~2.7 Ga), Abitibi Greenstone belt, Canada (Dostal and Mueller, 2013), Koolyanobbing greenstone belt (~3.0 Ga), Yilgarn Craton, Australia (Angerer et al., 2013), and Onverwacht suite (~3.5-3.3 Ga), Barberton greenstone belt, South Africa (Furnes et al., 2012). The field association, metamorphic grade, mineralogy and major elemental compositions of the komatiite-basalt suites in the BGB and the mentioned three Archean greenstone belts are very alike. While the Abitibi- and Koolyanobbing- greenstone belt contains both Al- depleted and -undepleted variety of komatiites along with other basalts, the Barberton greenstone belt contain mainly Al-undepleted variety of komatiite associated with basalts. Dostal and Mueller (2013) divided the volcanic assemblage of Stoughton-Rouemature group into two sets based on Al- and HREE- undepletion/depletion. They suggested that the different komatiites and basalts were generated by melting of different parts of a heterogeneous mantle plume and denied the possibility of basalt formation from komatiites by AFC processes. Similarly Angerer et al. (2013) suggested that the different volcanic rocks of Koolyanobbing greenstone belt were generated from a zoned plume and/or melting over a range of depths in a convergent plate margin setting. Furnes et al. (2012) also concluded that the komatiites and basalts of Onverwacht suite were generated by variable degrees of partial melting at different depths and temperatures of metasomatised mantle in a subduction zone setting.

When we plotted the data of komatiites and basalts present in these greenstone belts together in binary diagrams such as MgO-CaO, MgO-Ni, MgO-Zr and Zr-Yb (Fig.12), the basalts and komatiites formed continuous data array. They also showed olivine/orthopyroxene dominated fractional crystallization during the formation of komatiites (Fig. 12A), clinopyroxene dominated fractional crystallization during the formation of basalts (Fig. 12B), and incorporation of crustal components during the formation of basaltic melts (Fig. 12C and D) similar to the BGB rocks. Therefore, we propose that the different komatiites of these greenstone belts were possibly generated from different parts of heterogeneous sources, but the basalts were possibly evolved from the corresponding komatiites involving AFC processes similar to the BGB rocks. Most of the studies (e.g. Nesbitt and Sun, 1976; Arndt and Nesbitt, 1984; Arndt et al., 1997; Hanski et al., 2001; Furnes et al., 2012; Dostal and Mueller, 2013; Angerer et al., 2013; Verma et al., 2017) though suggest diverse origins of Archean komatiites and basalts, the possibility of a genetic connection among them cannot be completely ruled out. Therefore, a geochemical reinvestigation is needed to verify the rationality of the AFC model as an effective mechanism for basalt formation from komatiites in Archean greenstone belts.

8. Conclusions

The results and discussion led us to the following major conclusions. The melt of Al–depleted and –undepleted komatiites present in the BGB were originated by moderate–high degree melting of mantle plume at different depth. The melts further went through assimilation and olivine–orthopyroxene controlled fractional crystallization in magma chambers. The komatiitic basalts were mostly produced from clinopyroxene controlled fractional crystallization and assimilation of Al–undepleted komatiite melts formed by moderate degree melting of mantle plume. The tholeiitic basalts were generated by mostly clinopyroxene controlled fractional crystallization and assimilation of more evolved komatiitic basalt and primitive tholeiitic basalt melts. The Older Metamorphic Tonalitic Gneiss and third phase of Singhbhum Granite Type–A were the basement of the Badampahar greenstone belt (BGB) rocks and they contributed sediments for metaconglomerate and contaminated the magma. The newly discovered older age limit of the BGB rocks is 3.25 Ga which is 50 Ma younger than the previously reported age limit. The formation of the BGB rocks is confined between 3.25 Ga and 3.1 Ga.

Acknowledgements

The research work was supported by Council of Scientific and Industrial Research (India) research fellowship of R. Ghosh. We are grateful to the handling editor and the reviewers for their meticulous review and constructive comments on the previous version of our manuscript. Sincere thanks are due to Prof. Sisir Kanti Mondal of the Dept. of Geological Sciences, Jadavpur University for constructive discussion and suggestions while preparing the manuscript. The authors are also grateful to Dr. Shiladitya Sengupta and other co–workers of petrology laboratory, Geological Survey of India for their support during zircon sample preparation.

References

Acharyya, S. K., Gupta, A., Orihashi, Y., 2010. New U-Pb zircon ages from Paleo-Mesoarchean TTG gneisses of the Singhbhum Craton, eastern India. Geochemical Journal, 44(2), 81-88.

Angerer, T., Kerrich, R., Hagemann, S.G., 2013. Geochemistry of a komatiitic, boninitic, and tholeiitic basalt association in the Mesoarchean Koolyanobbing greenstone belt, Southern Cross Domain, Yilgarn craton: Implications for mantle sources and geodynamic setting of banded iron formation. Precambrian Research, 224, 110-128.

Arndt, N. T., 1991. High Ni in Archean tholeiites. Tectonophysics, 187(4), 411-419.

Arndt, N. T., Naldrett, A. J., Pyke, D. R., 1977. Komatiitic and iron-rich tholeiitic lavas of Munro Township, northeast Ontario. Journal of Petrology,18(2), 319-369.

Arndt, N.T., Nesbitt, R.W., 1982. Geochemistry of Munro Township Basalt In, Arndt, N.T. and Nisbet, E.G. (eds.) Komatiites. London, GB, George Allen & Unwin, pp. 309-329.

Arndt, N. T., Nesbitt, R. W., 1984. Magma mixing in komatiitic lavas from Munro Township, Ontario. In Archaean Geochemistry (pp. 99-114). Springer, Berlin, Heidelberg.

Arndt, N.T., Teixeira, N.A., White, W.M., 1989. Bizarre geochemistry of komatiites from the Crixas greenstone belt, Brazil. Contributions to Mineralogy and Petrology, 101(2),187-197.

Arndt, N.T., Kerr, A.C., Tarney, J., 1997. Dynamic melting in plume heads: the formation of Gorgona komatiites and basalts. Earth and Planetary Science Letters, 146(1), 289-301.

Arndt, N., Lesher, M., Barnes, S., 2008. Komatiite (p. 487). Cambridge university press.

Barnes, S.J., HILL, R.E., GOLE, M.J., 1988. The Perseverance ultramafic complex, Western Australia: the product of a komatiite lava river. Journal of Petrology, 29(2), 305-331.

Barnes, S. J., 2000, Chromite in komatiites, II. Modification during greenschist to mid-amphibolite facies metamorphism. Journal of Petrology, 41(3), 387-409.

Campbell, I. H., Griffiths, R. W., Hill, R. I., 1989. Melting in an Archaean mantle plume: heads it's basalts, tails it's komatiites. Nature, 339(6227), 697.

Cattell, A., 1987. Enriched komatiitic basalts from Newton Township, Ontario: their genesis by crustal contamination of depleted komatiite magma. Geological Magazine, 124(4), 303-309.

Chaudhuri, T., Mazumder, R., Arima, M., 2015. Petrography and geochemistry of

Mesoarchaean komatiites from the eastern Iron Ore belt, Singhbhum craton, India, and its similarity with ‘Barberton type komatiite’. J. Afr. Earth Sci. 101 (2015), 135–147.

Chaudhuri, T., Satish-Kumar, M., Mazumder, R., Biswas, S., 2017. Geochemistry and Sm-Nd isotopic characteristics of the Paleoarchean Komatiites from Singhbhum Craton, Eastern India and their implications. Precambrian Research, 298, 385-402.

Condie, K. C., 1994, Greenstones through time. In Developments in Precambrian Geology (11, 85-120). Elsevier.

Condie, K.C., 2015. Earth as an evolving planetary system. Academic Press.

Condie, K.C., Aster, R.C., van Hunen, J., 2016. A great thermal divergence in the mantle beginning 2.5 Ga: geochemical constraints from greenstone basalts and komatiites. Geoscience Frontiers, 7(4), 543-553.

Dostal, J., Mueller, W.U., 2013. Deciphering an Archean mantle plume: Abitibi greenstone belt, Canada. Gondwana Research, 23(2), 493-505.

Ersoy, E. Y., 2013, PETROMODELER (Petrological Modeler): a Microsoft® Excel© spreadsheet program for modelling melting, mixing, crystallization and assimilation processes in magmatic systems. Turkish Journal of Earth Sciences, 22(1), 115-125.

Francis, D. M., Hynes, A. J., 1979. Komatiite-derived tholeiites in the Proterozoic of New Quebec. Earth and Planetary Science Letters, 44(3), 473-481.

Furnes, H., Robins, B., de Wit, M.J., 2012. Geochemistry and petrology of lavas in the upper Onverwacht Suite, Barberton Mountain Land, South Africa. South African Journal of Geology, 115(2), 171-210.

Garzanti, E., Vermeesch, P., Rittner, M., Simmons, M., 2018. The zircon story of the Nile: time-structure maps of source rocks and discontinuous propagation of detrital signals. Basin Research.

Ghosh, D., Sarkar, S.N., Saha, A.K., Ray, S.L., 1996. New insights on the early Archaean crustal evolution in eastern India: re-evaluation of lead-lead, samarium-neodymium and rubidium-strontium geochronology. Ind. Minerals, 50, 175-188.

Ghosh, R., & Baidya, T. K., 2017a. Mesoarchean BIF and iron ores of the Badampahar greenstone belt, Iron Ore Group, East Indian Shield. Journal of Asian Earth Sciences, 150, 25-44.

Ghosh, R., Baidya, T. K., 2017b. Using BIF magnetite of the Badampahar greenstone belt, Iron Ore Group, East Indian Shield to reconstruct the water chemistry of a 3.3–3.1 Ga sea during iron oxyhydroxides precipitation. Precambrian Research, 301, 102-112.

Goswami, J. N., Mishra, S., Wiedenbeck, M., Ray, S. L., Saha, A. K., 1995. 3.55 Ga old zircon from Singhbhum–Orissa iron ore craton, eastern India. *Current Science*, 1008-1012.

Green, D. H., 1975. Genesis of Archean peridotitic magmas and constraints on Archean geothermal gradients and tectonics. Geology, 3(1), 15-18.

Griffin, W., Powell, W., Pearson, N., O’Reilly, S., 2008. GLITTER: data reduction software for laser ablation ICP-MS. Laser Ablation-ICP-MS in the earth sciences. Mineralogical Association of Canada short course series, 40, 204–207.

Hanski, E., Huhma, H., Rastas, P., & Kamenetsky, V. S., 2001. The Palaeoproterozoic komatiite–picrite association of Finnish Lapland. Journal of Petrology, 42(5), 855-876.

Herzberg, C., 1992. Depth and degree of melting of komatiites. Journal of Geophysical Research: Solid Earth, 97(B4), 4521-4540.

Herzberg, C. T., Ohtani, E., 1988. Origin of komatiite at high pressures. Earth and Planetary Science Letters, 88(3-4), 321-329.

Hofmann, A.W., 1997. Mantle geochemistry: the message from oceanic volcanism. Nature, 385(6613), 219.

Irvine, T.N.J., Baragar, W.R.A.F., 1971. A guide to the chemical classification of the common volcanic rocks. Canadian journal of earth sciences, 8(5), 523-548.

Jayananda, M., Kano, T., Peucat, J.J., Channabasappa, S., 2008. 3.35 Ga komatiite volcanism in the western Dharwar craton, southern India: constraints from Nd isotopes and whole-rock geochemistry. Precambrian Research, 162(1), 160-179.

Jensen, L. S., 1976. A new cation plot for classifying subalkalic volcanic rocks (66). Ministry of Natural Resources.

Kinzler, R. J., 1997. Melting of mantle peridotite at pressures approaching the spinel to garnet transition: Application to mid-ocean ridge basalt petrogenesis. Journal of Geophysical Research: Solid Earth, 102(B1), 853-874.

Konnunaho, J.P., Hanski, E.J., Bekker, A., Halkoaho, T.A.A., Hiebert, R.S., Wing, B.A., 2013. The Archean komatiite-hosted, PGE-bearing Ni–Cu sulfide deposit at Vaara, eastern Finland: evidence for assimilation of external sulfur and post-depositional desulfurization. Mineralium Deposita, 48(8), 967-989.

Lassiter, J.C., DePaolo, D.J., 1997. Plume/lithosphere interaction in the generation of continental and oceanic flood basalts: chemical and isotopic constraints. Geophysical Monograph-American Geophysical Union, 100, 335-356.

Le Bas, M. J., 2000. IUGS reclassification of the high-Mg and picritic volcanic rocks. Journal of Petrology, 41(10), 1467-1470.

Le Bas, M. J., Maitre, R. L., Streckeisen, A., Zanettin, B., IUGS Subcommission on the Systematics of Igneous Rocks, 1986. A chemical classification of volcanic rocks based on the total alkali-silica diagram. Journal of petrology, 27(3), 745-750.

Maas, R., Kinny, P. D., Williams, I. S., Froude, D. O., Compston, W., 1992. The Earth's oldest known crust: a geochronological and geochemical study of 3900–4200 Ma old detrital zircons from Mt. Narryer and Jack Hills, Western Australia. Geochimica et Cosmochimica Acta, 56(3), 1281-1300.

Maitre, L., 1989. A classification of igneous rocks and glossary of terms. Recommendations of the international union of geological sciences subcommission on the systematics of igneous rocks, 193.

Mishra, S., Deomurari, M. P., Wiedenbeck, M., Goswami, J. N., Ray, S., Saha, A. K., 1999. 207Pb/206Pb zircon ages and the evolution of the Singhbhum Craton, eastern India: an ion microprobe study1. Precambrian Research, 93(2-3), 139-151.

Mole, D.R., Fiorentini, M.L., Thebaud, N., Cassidy, K.F., McCuaig, T.C., Kirkland, C.L., Romano, S.S., Doublier, M.P., Belousova, E.A., Barnes, S.J., Miller, J., 2014. Archean komatiite volcanism controlled by the evolution of early continents. Proceedings of the National Academy of Sciences, 111(28), 10083-10088.

Mukhopadhyay, D., 2001. The Archaean nucleus of Singhbhum: the present state of knowledge. Gondwana Research, 4(3), 307-318.

Murray, R.W., Miller, D.J., Kryc, K.A., 2000, Analysis of major and trace elements in rocks, sediments, and interstitial waters by inductively coupled plasma–atomic emission spectrometry (ICP-AES).

Nelson, D. R., Bhattacharya, H. N., Thern, E. R., Altermann, W., 2014. Geochemical and ion-microprobe U–Pb zircon constraints on the Archaean evolution of Singhbhum Craton, eastern India. Precambrian Research, 255, 412-432.

Nesbitt, R. W., Sun, S. S., 1976. Geochemistry of Archaean spinifex-textured peridotites and magnesian and low-magnesian tholeiites. Earth and Planetary Science Letters, 31(3), 433-453.

Palme, H., O'Neill, H., 2014. Cosmochemical estimates of mantle composition. In Treatise on Geochemistry, 2nd Edition. Elsevier.

Pearce, J. A., 1996. A user's guide to basalt discrimination diagrams. Trace element geochemistry of volcanic rocks: applications for massive sulphide exploration. Geological Association of Canada, Short Course Notes, 12(79), 113.

Polat, A., Kerrich, R., 2000. Archean greenstone belt magmatism and the continental growth–mantle evolution connection: constraints from Th–U–Nb–LREE systematics of the 2.7 Ga Wawa subprovince, Superior Province, Canada. Earth and Planetary Science Letters, 175(1), 41-54.

Qing, C., Shibata, T., Shinotsuka, K., Yoshikawa, M., Tatsumi, Y., 2003. Precise determination of trace elements in geological standard rocks using inductively coupled plasma mass spectrometry (ICP-MS). *Frontier Research on Earth Evolution: IFREE Report for...*, *1*, pp.357.

Saha, A. K., 1994, M-27. Crustal Evolution of Singhbhum-North Orissa, Eastern India. GSI Publications, 1(1).

Sahu, N.K., Mukherjee, M.M., 2001. Spinifex textured komatiite from Badampahar-Gorumahisani schist belt, Mayurbhanj District, Orissa. J. Geol. Soc. India 57, 529–534.

Sengupta, S., Corfu, F., McNutt, R.H., Paul, D.K., 1996. Mesoarchaean crustal history of the eastern Indian craton: Sm-Nd and U-Pb isotopic evidence. Precambrian Research, 77, 17-22.

Smithies, R.H., Champion, D.C., Sun, S.S., 2004. The case for Archaean boninites. Contributions to Mineralogy and Petrology, 147(6), 705-721.

Stiegler, M.T., Lowe, D.R., Byerly, G.R., 2010. The petrogenesis of volcaniclastic komatiites in the Barberton greenstone belt, South Africa: A textural and geochemical study. Journal of Petrology, 51(4), 947-972.

Sun, S. S., McDonough, W. S., 1989. Chemical and isotopic systematics of oceanic basalts: implications for mantle composition and processes. Geological Society, London, Special Publications, 42(1), 313-345.

Sun, S. S., Nesbitt, R. W., 1978. Geochemical regularities and genetic significance of ophiolitic basalts. Geology, 6(11), 689-693.

Taylor, S. R., McLennan, S. M., 1985. The continental crust: Its evolution and composition. Lon on: Blackwell.

Upadhyay, D., Chattopadhyay, S., Kooijman, E., Mezger, K., Berndt, J., 2014. Magmatic and metamorphic history of Paleoarchean tonalite–trondhjemite–granodiorite (TTG) suite from the Singhbhum craton, eastern India. Precambrian research, 252, 180-190.

Vermeesch, P., 2012. On the visualisation of detrital age distributions. Chemical Geology, 312-313, 190–194.

Vermeesch, P., 2018. IsoplotR: a free and open toolbox for geochronology. Geoscience Frontiers. Geophysical research abstracts, 20.

Verma, S.K., Oliveira, E.P., Silva, P.M., Moreno, J.A., Amaral, W.S., 2017. Geochemistry of komatiites and basalts from the Rio das Velhas and Pitangui greenstone belts, São Francisco Craton, Brazil: Implications for the origin, evolution, and tectonic setting. Lithos, 284, 560-577.

Walter, M. J., 1998. Melting of garnet peridotite and the origin of komatiite and depleted lithosphere. Journal of Petrology, 39(1), 29-60.

Waterton, P., Pearson, D.G., Kjarsgaard, B., Hulbert, L., Locock, A., Parman, S., Davis, B., 2017. Age, origin, and thermal evolution of the ultra-fresh~ 1.9 Ga Winnipegosis Komatiites, Manitoba, Canada. Lithos, 268, 114-130.

Table 1. Early to middle Archean stratigraphic sequence of rocks in the Singhbhum Craton, modified after Saha (1994).

Stratiraphic unit	Events	Major lithologies	Age (Ga)	References
	Metamorphism of OMG, OMTG and SBG		3.02-2.96, 2.52 and 1.06	Upadhyay et al. (2014)
Mayurbhanj Granite	Emplacement of granitic pluton	Granite	3.09-3.08	Mishra et al. (1999)
SBG Type-B		Granodiorite to granite	3.12	Ghosh et al. (1996)
Bonai granite		Granite to granodiorite	3.16	Sengupta et al. (1991)
	Metamorphism of SBG Type-A, OMTG and OMG		3.19 - 3.13	Upadhyay et al. (2014)
Iron Ore Group	Deposition and metamorphism of Iron ore group of rocks	Mafic to felsic volcanic rocks, tuff, banded iron formations, local dolomite, quartzitic sandstone and conglomerate	3.3-3.1	Saha (1994)
---Unconformity---				
	Metamorphism of SBG Type-A, OMTG and OMG		3.24 3.34 - 3.26	Mishra et al. (1999) Upadhyay et al. (2014)
SBG Type-A:	Emplacement of granitic pluton	Granite, tonalite and granodiorite		
Third phase			3.33 3.32	Upadhyay et al. (2014) Mishra et al. (1999)
Second phase			3.35	Upadhyay et al. (2014)
First phase			3.44	Upadhyay et al. (2014)
	Metamorphism of OMG and OMTG		3.40	Mishra et al. (1999)
OMTG granite		Granite	3.32	Upadhyay et al. (2014)
OMTG	Intrusion of tonalite-trondhjemite-granodiorite rocks in OMG	Tonalite gneiss and granodiorite	3.44 and 3.52 3.45 - 3.43 3.45 - 3.44	Acharyya et al. (2010) Mishra et al. (1999) Upadhyay et al. (2014)
OMG	Deposition of sediments with mafic volcanism	Amphibolites, pelitic schists, banded calc-gneiss	3.55-3.44	Mishra et al. (1999)
---Unconformity---				
Unpreserved primitive crust represented by xenocrystic zircons present in younger rocks			3.61 3.6-3.55	Upadhyay et al. (2014) Goswami et al. (1995)

OMG ~ Older Metamorphic Group; OMTG ~ Older Metamorphic Tonalite Gneiss; SBG ~ Singhbhum Granite

Table 2. Summary of U-Pb isotope data and concordant ages of zircons extracted from conglomerate sample from the Badampahar greenstone belt, Singhbhum Craton, Eastern India..

sample	U [ppm]	Th [ppm]	Th/U	Pb207/U235	Error [sigma]	Pb206/U238	Error [sigma]	Age [Ma]	Error [sigma]
A33_G001	104.1343	52.01426	0.499492	29.30901	0.38289	0.71769	0.00869	3450.8	18.35
A33_G002	47.04545	33.60212	0.714248	24.86315	0.34316	0.66811	0.0085	3305.9	19.65
A33_G003	186.0674	79.70595	0.428371	30.46304	0.39138	0.72639	0.00863	3492	18.01
A33_G005	263.2431	111.3827	0.423117	29.40719	0.37692	0.70504	0.00833	3483.5	18.01
A33_G006	66.60367	56.89796	0.854277	28.88105	0.39074	0.69636	0.00869	3474.8	19.02
A33_G007	394.8646	132.0472	0.334411	23.9905	0.31114	0.65166	0.00776	3289	18.54
A33_G008	45.45965	32.86208	0.722885	24.74461	0.35025	0.66697	0.00863	3301.1	20.23
A33_G009	283.3299	204.1078	0.720389	30.66653	0.39715	0.73536	0.00871	3483.3	18.26
A33_G010	164.3948	93.63589	0.569579	25.43896	0.33469	0.68373	0.0082	3305.5	18.83
A33_G011	135.3217	93.53097	0.691175	25.43139	0.33774	0.68305	0.00825	3306.6	19.02
A33_G012	468.8687	483.3699	1.030928	26.54442	0.34511	0.6574	0.00775	3433.2	18.48
A33_G014	56.03166	70.02496	1.249739	26.72357	0.37403	0.70462	0.0089	3335.6	20.03
A33_G015	190.8248	200.6497	1.051486	28.57959	0.3809	0.68945	0.00826	3473.9	18.94
A33_G016	100.4341	71.91305	0.716022	25.4913	0.34873	0.68568	0.0084	3304.3	19.71
A33_G019	168.095	87.76032	0.522088	29.87107	0.40772	0.72424	0.00876	3466.1	19.5
A33_G020	238.9274	364.6439	1.52617	22.86883	0.31422	0.62605	0.00757	3276.7	19.98
A33_G021	367.3774	161.3777	0.43927	23.93766	0.32632	0.66661	0.00796	3249.8	19.89
A33_G027	269.5863	260.7481	0.967216	26.20556	0.37209	0.6646	0.00804	3396.3	20.67
A33_G028	205.097	212.4439	1.035822	27.49039	0.39488	0.68873	0.0084	3415.3	20.9
A33_G032	213.026	145.714	0.68402	28.5462	0.40431	0.69486	0.0082	3460	21.1
A33_G033	178.667	86.54671	0.484402	30.3289	0.43435	0.72634	0.00867	3485.2	21.27
A33_G034	200.8682	240.1618	1.195619	25.23124	0.36153	0.62945	0.00748	3421.9	21.46
A33_G035	169.1522	204.8402	1.210982	32.38192	0.51754	0.77549	0.01055	3485.2	23.28
A33_G036	191.3534	127.8454	0.668111	30.4084	0.4369	0.73712	0.00874	3466.4	21.44
A33_G0	264.30	236.12	0.8934	29.924	0.427	0.7177	0.00839	3482	21.39

38	03	97	14	45	68	5		.8	
A33_G040	201.3968	195.6796	0.971612	24.85014	0.36207	0.668	0.00792	3305.3	22.13
A33_G042	219.3692	95.85115	0.43694	30.60499	0.44628	0.73448	0.00867	3481.9	21.88
A33_G043	84.04749	33.18192	0.3948	30.45062	0.46588	0.72962	0.00913	3484.4	22.78
A33_G044	294.4305	297.2225	1.009483	27.68208	0.40393	0.67672	0.00792	3453.3	22.03
A33_G045	186.596	140.3023	0.751904	28.01275	0.43988	0.69871	0.00896	3422.1	23.5
A33_G047	304.4739	207.8299	0.682587	23.46446	0.34686	0.64688	0.00757	3265.6	22.72
A33_G048	278.0439	433.0343	1.557432	25.05668	0.3716	0.619	0.00725	3437	22.53
A33_G050	192.9392	165.8804	0.859755	27.11344	0.40828	0.65605	0.00778	3469.2	22.82
A33_G052	213.5546	262.0518	1.227095	24.90894	0.37932	0.67449	0.00802	3293.8	23.42
A33_G054	136.9075	80.17241	0.585595	25.93884	0.40217	0.703	0.00848	3292.4	23.84
A33_G056	40.17364	31.83269	0.792377	25.20021	0.44469	0.68299	0.00967	3292.4	26.67
A33_G057	114.1777	61.04321	0.534633	30.47358	0.48791	0.72013	0.00888	3505.9	24.27
A33_G059	49.68845	34.08573	0.685989	24.60864	0.4183	0.66283	0.00874	3302.2	26.05
A33_G061	274.3437	113.6353	0.414208	29.11804	0.45937	0.70098	0.00823	3477.2	24.25
A33_G062	50.74565	23.61573	0.465374	29.3856	0.50547	0.70532	0.00938	3481.9	26
A33_G063	218.312	119.594	0.547812	23.72912	0.38108	0.62066	0.00738	3348.2	24.96
A33_G064	224.1266	150.0933	0.669681	25.44427	0.41032	0.62401	0.00743	3448.5	24.9
A33_G065	156.4658	88.59502	0.566226	27.97791	0.45752	0.6719	0.00812	3481	25.15
A33_G069	250.5567	146.8372	0.586044	26.02827	0.42744	0.6324	0.00748	3463.1	25.49
A33_G070	66.07507	30.46045	0.460998	29.08745	0.50877	0.69062	0.00899	3498.8	26.73
A33_G071	110.4775	47.08095	0.426159	29.30418	0.49963	0.6944	0.00862	3501.8	26.25
A33_G073	228.884	321.5561	1.404887	27.57275	0.46262	0.66581	0.00791	3472.7	26.11
A33_G076	205.097	92.83587	0.452644	27.3131	0.46575	0.65167	0.00778	3491.3	26.57
A33_G079	75.58988	51.03224	0.67512	23.45886	0.41953	0.63368	0.00799	3298.1	28.18
A33_G080	247.9137	122.6371	0.494677	25.27431	0.4399	0.61945	0.00741	3449.8	27.32
A33_G081	31.18743	21.88916	0.701858	24.33192	0.47092	0.65242	0.0092	3309.7	30.1
A33_G083	26.43003	22.78724	0.862172	24.13599	0.48321	0.6476	0.00951	3308.7	31.06

Table 3. Ratios and anomalies of rare earth elements in the BGB metavolcanic rocks and other modern standard volcanic rocks.

		$(La/Sm)_{CI}$	$(Gd/Yb)_{CI}$	$(La/Yb)_{CI}$	$(Eu/Eu^*)_{CI}$	$(La/Sm)_{NM}$	$(Gd/Yb)_{NM}$	$(La/Yb)_{NM}$	$(Ce^*/Ce)_{CI}$	Mg#	Al_2O_3/TiO_2	CaO/Al_2O_3
Komatiites	**E35**	bdl	0.453	bdl	0.988	bdl	0.454	bdl	bdl	75.0	61.6	0.369
	D-84	2.28	2.68	9.04	0.939	3.72	2.68	15.4	0.856	56.2	2.43	4.20
	E32	2.25	2.20	7.79	0.820	3.67	2.20	13.2	0.764	61.6	4.86	1.08
	E25	0.849	1.20	0.854	1.27	1.38	1.20	1.45	0.795	59.9	18.5	2.14
	E24	1.25	0.632	0.598	1.04	2.04	0.633	1.02	0.756	65.0	61.6	0.767
	D118	1.92	2.08	4.58	0.949	3.12	2.08	7.79	0.978	60.5	7.07	1.06
	D120	2.45	1.38	3.59	1.00	3.99	1.38	6.10	0.991	59.7	12.9	1.41
Komatiitic basalts	**E34**	0.856	1.06	0.784	0.802	1.40	1.06	1.33	0.964	39.4	27.4	1.02
	E39	1.16	1.65	1.86	0.923	1.89	1.65	3.16	0.991	33.1	9.78	1.26
	E36	0.788	1.54	1.09	1.03	1.28	1.55	1.86	1.00	45.8	11.6	1.87
	E37	0.856	1.52	1.24	1.01	1.39	1.52	2.11	0.994	42.6	10.5	1.74
	E40	1.01	1.97	2.15	1.05	1.64	1.98	3.66	0.934	35.1	7.35	1.93
	E44	1.05	1.63	1.68	1.02	1.72	1.63	2.85	0.952	40.7	10.6	1.44
	E38	1.03	1.64	1.67	1.05	1.06	1.14	1.14	1.03	20.8	10.8	0.600
	A-10	0.651	1.14	0.669	0.874	3.64	1.67	6.87	1.03	31.6	9.38	1.27
	D11	2.24	1.67	4.04	1.03	3.44	1.23	4.27	0.966	41.0	17.9	1.08
	E23	0.956	1.21	0.936	0.994	1.56	1.22	1.59	1.13	50.4	17.6	1.61
	D123	1.47	1.60	2.68	0.970	2.40	1.60	4.55	1.03	42.7	13.1	1.08
	A26	1.25	1.09	1.21	0.938	2.04	1.09	2.05	0.914	45.0	21.7	1.05
Tholeiitic basalts	**D33**	1.65	1.60	2.98	0.991	2.70	1.60	5.06	0.982	25.1	12.1	0.875
	E11	1.95	1.19	2.31	0.908	3.18	1.20	3.92	0.960	24.9	10.7	0.464
	E13	1.97	1.21	2.35	0.869	3.21	1.21	4.00	0.977	23.1	10.9	0.606
	E17	2.11	1.20	2.51	0.909	1.68	1.64	2.84	0.979	39.4	12.1	1.63
	E22	2.13	1.35	3.21	0.863	3.48	1.35	5.45	0.990	19.6	6.81	0.708

	D111	3.55	1.45	5.98	0.791	5.78	1.45	10.2	0.907	15.4	13.5	0.510
others	**PM**	1.00	1.00	1.00	0.998	1.63	1.00	1.70	-	-	-	-
	NM	0.614	0.998	0.588	1.00	1.00	1.00	1.00	-	-	-	-
	EM	1.56	1.04	1.91	1.00	2.55	1.04	3.24	-	-	-	-

[CI] ~ CI chondrite normalized; [NM]~ NMORB normalized; bdl~ below detection limit; [a] ~ Ghosh and Baidya (2017b); [b] ~ Sun & McDonough (1989); PM ~ average primitive mantle; NM~ average NMORB; EM~ average EMORB

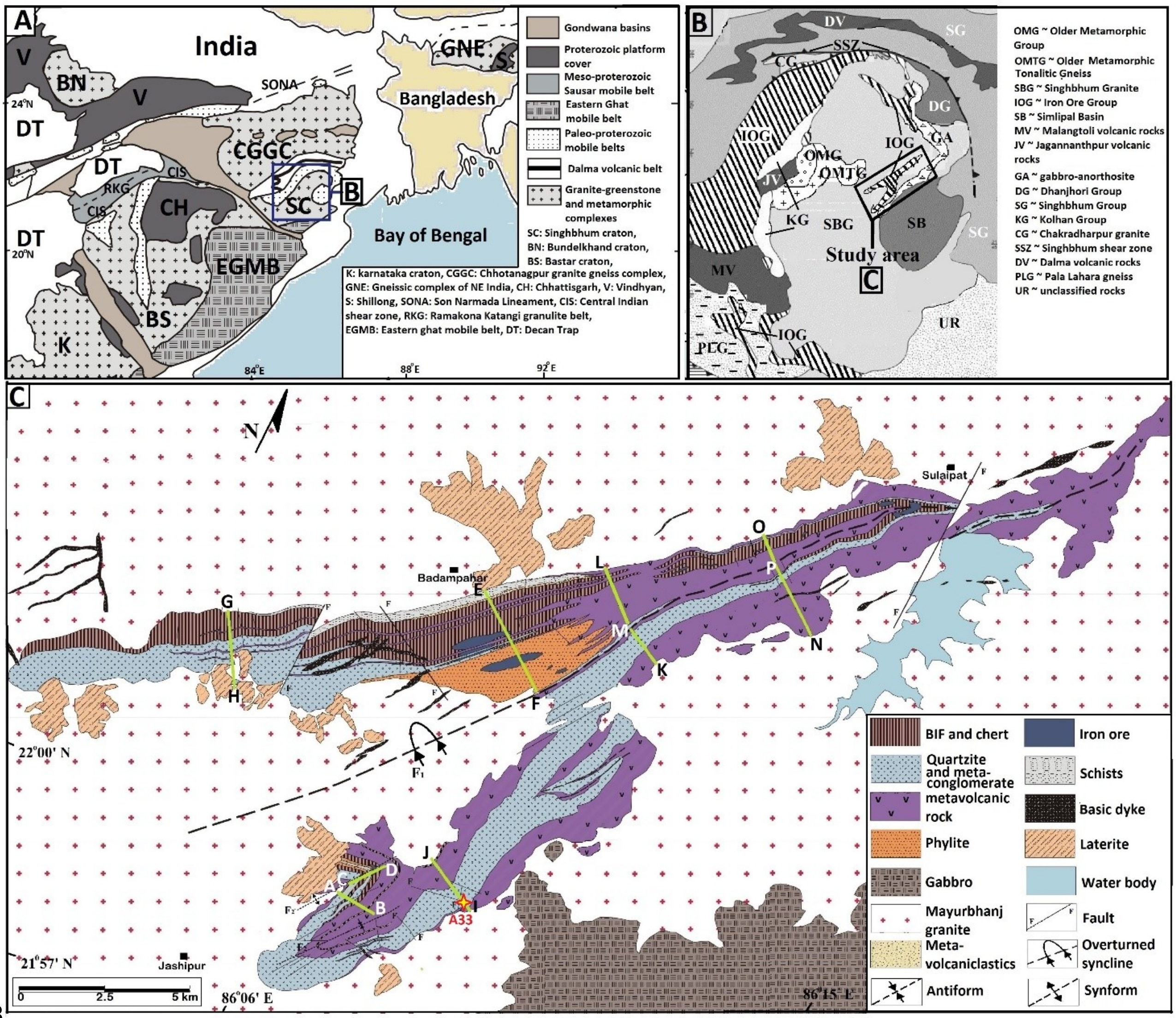

Fig. 1. (A) Geological map of India showing locations of major Precambrian terrains (modified after Acharyya, 2002). (**B)** Enlarged view of the Singhbhum Craton with the spatial distribution of different stratigraphic units (modified after Saha, 1994). (**C)** Geological map of the Badampahar greenstone Belt, Singhbhum craton (after Ghosh and Baidya, 2017b). Location (N22°00’15”, E86°08’40”) of the dated metaconglomerate sample (A33) is marked.

779 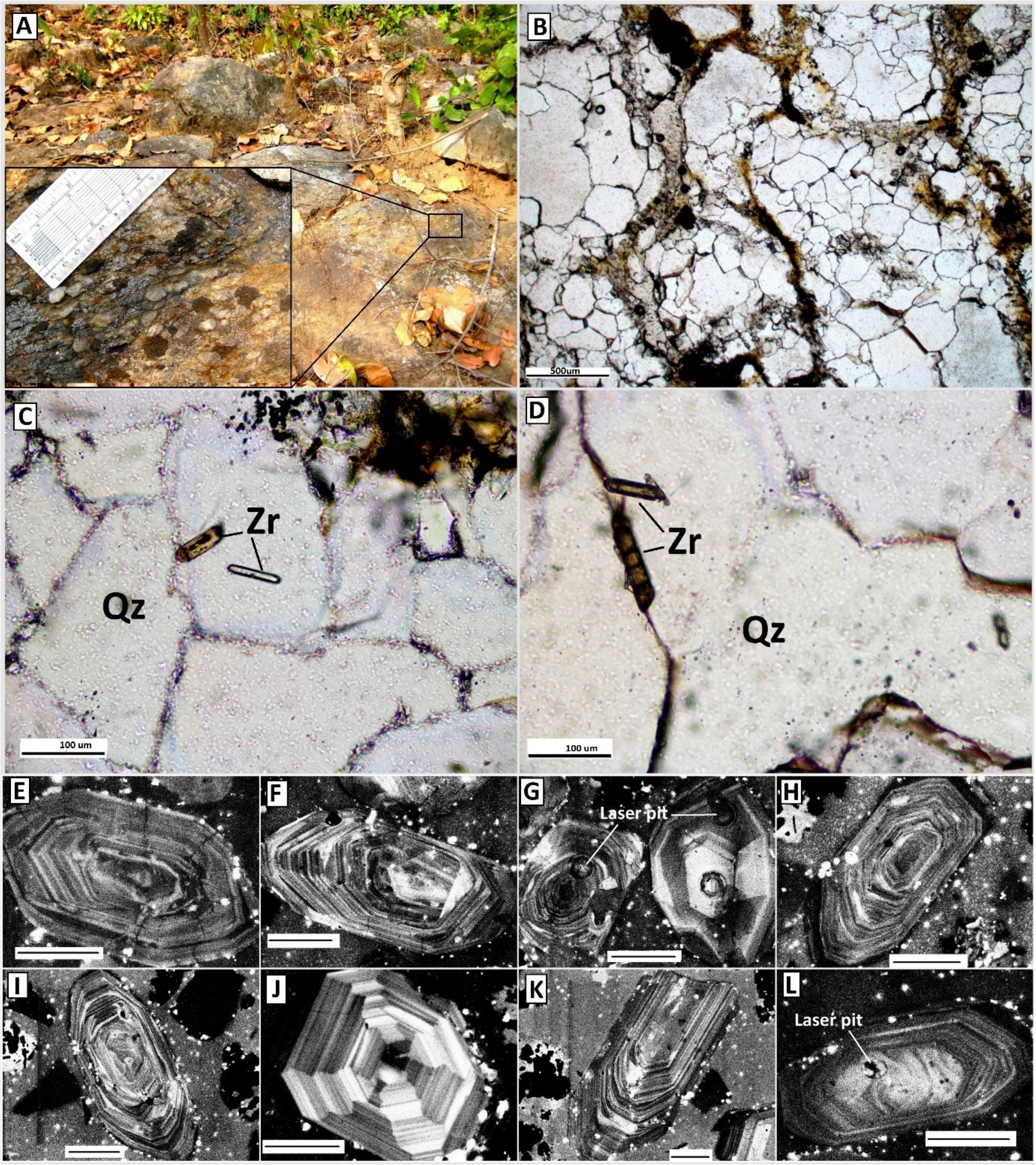
A
B
500um
C
Zr
Qz
100 um
D
Zr
Qz
100 um
E
F
G
Laser pit
H
I
J
K
L
Laser pit

Fig. 2. (A) Outcrop of metaconglomerate (A33) at the southern limb of BGB syncline. (**B), (C) & (D)** Photomicrographs show ellipsoidal clasts of metaconglomerate consisting mostly quartz crystals. The contact of quartz crystals are mostly sharp and straight. Inclusions of zircon are present within quartz. (**E)-(L)** CL images of analysed zircon grains showing oscillatory growth zoning.

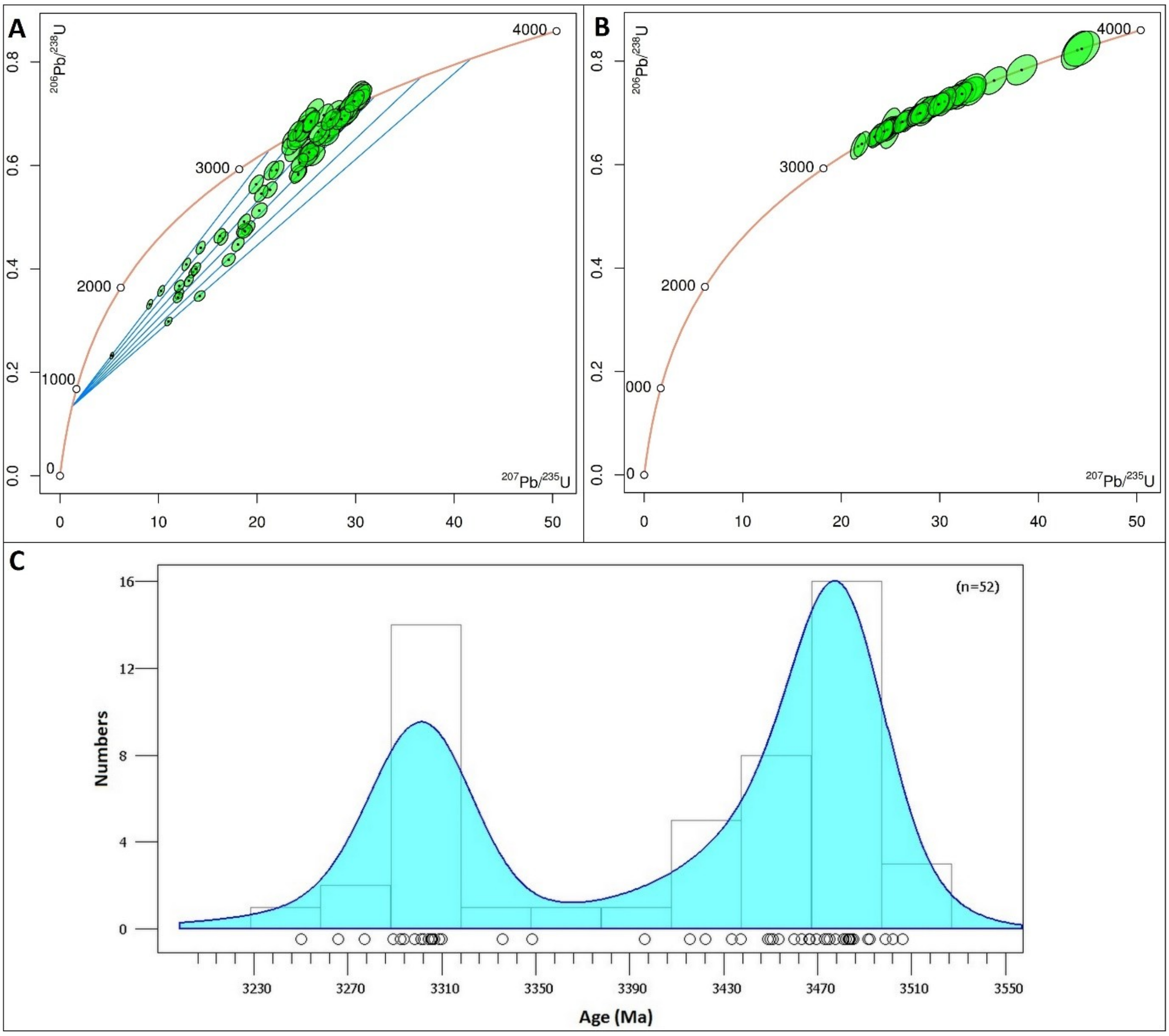

Fig. 3. (A) Wetherill concordia diagram of metaconglomerate sample A33, suggesting Archaean protolith ages and a Neoproterozoic partial resetting event. Blue lines mark the trajectory of the Pb-loss. (**B)** Assuming initial concordance, the original U-Pb compositions may be restored by projecting the data back to the concordia line. (**C)** Kernel Density Estimate (KDE) of the zircons having concordant ages.

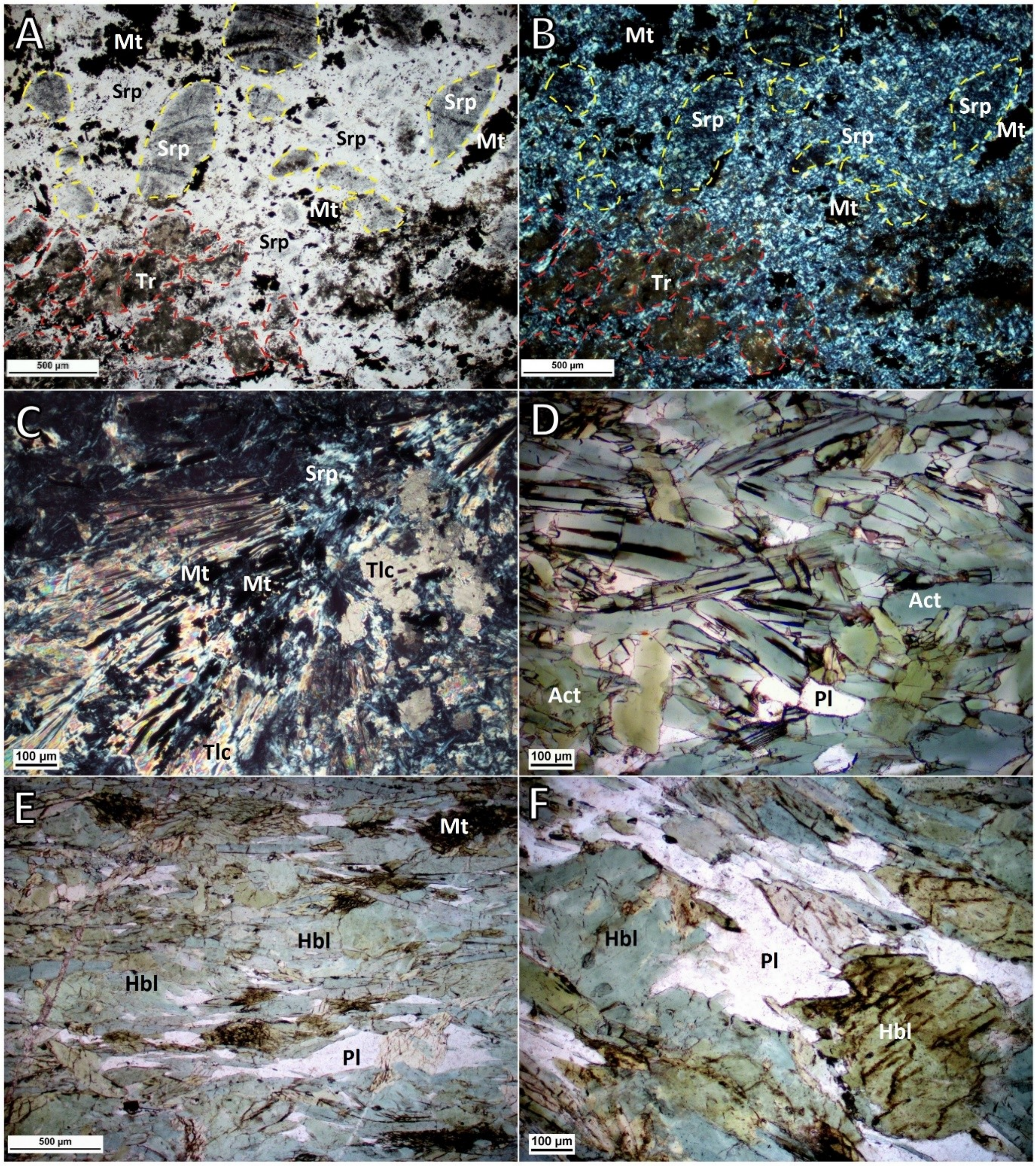

Fig. 4. Photomicrographs of metavolcanic rocks in the Badampahar greenstone belt, Singhbhum Craton. **(A)** and **(B)** Serpentine (Srp) and tremolite (Tr) pseudomorphs (marked by yellow and red dotted lines, respectively) after original igneous minerals along with magnetite (Mt) crystals represent relic cumulate texture in a 'meta' komatiite. **(C)** Relic spinifex texture in a 'meta' komatiite represented by acicular radiating crystals of magnetite and Tlc-Srp pseudomorphs after olivine/orthopyroxene. (**D)** Actinolite (Act) and plagioclase in a 'meta' komatiitic basalt showing crude alignment along regional S_1 foliation. (**E)** Hornblende (Hbl) and Pl crystals of a 'meta' tholeiitic basalt aligned along the S_1 foliation.

(F) Relic ophitic and subophitic texture represented by the outline of Hbl and Pl crystals in a ‘meta’ tholeiitic basalt.

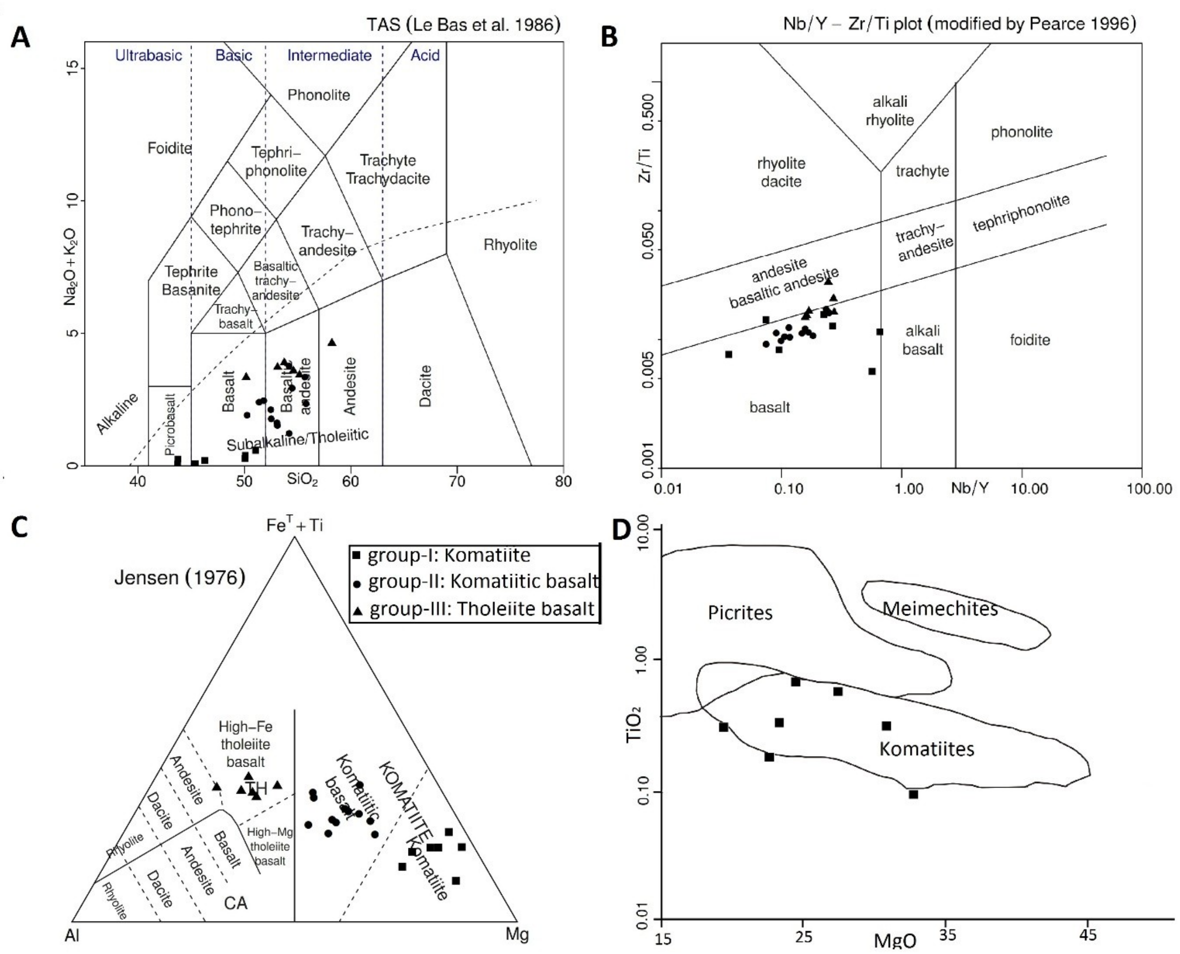

Fig. 5. The metavolcanic rocks of BGB are plotted in (**A**) SiO_2 vs. K_2O+Na_2O diagram (after Le Bas et al., 1986), (**B**) Nb/Y vs. Zr/Ti diagram (after Pearce, 1996), (**C**) Mg-Fe+Ti-Al triangular diagram (Jensen, 1976). (**D**) High Mg group-I rocks of the BGB plotted in MgO-TiO_2 diagram (after Arndt et al., 2008).

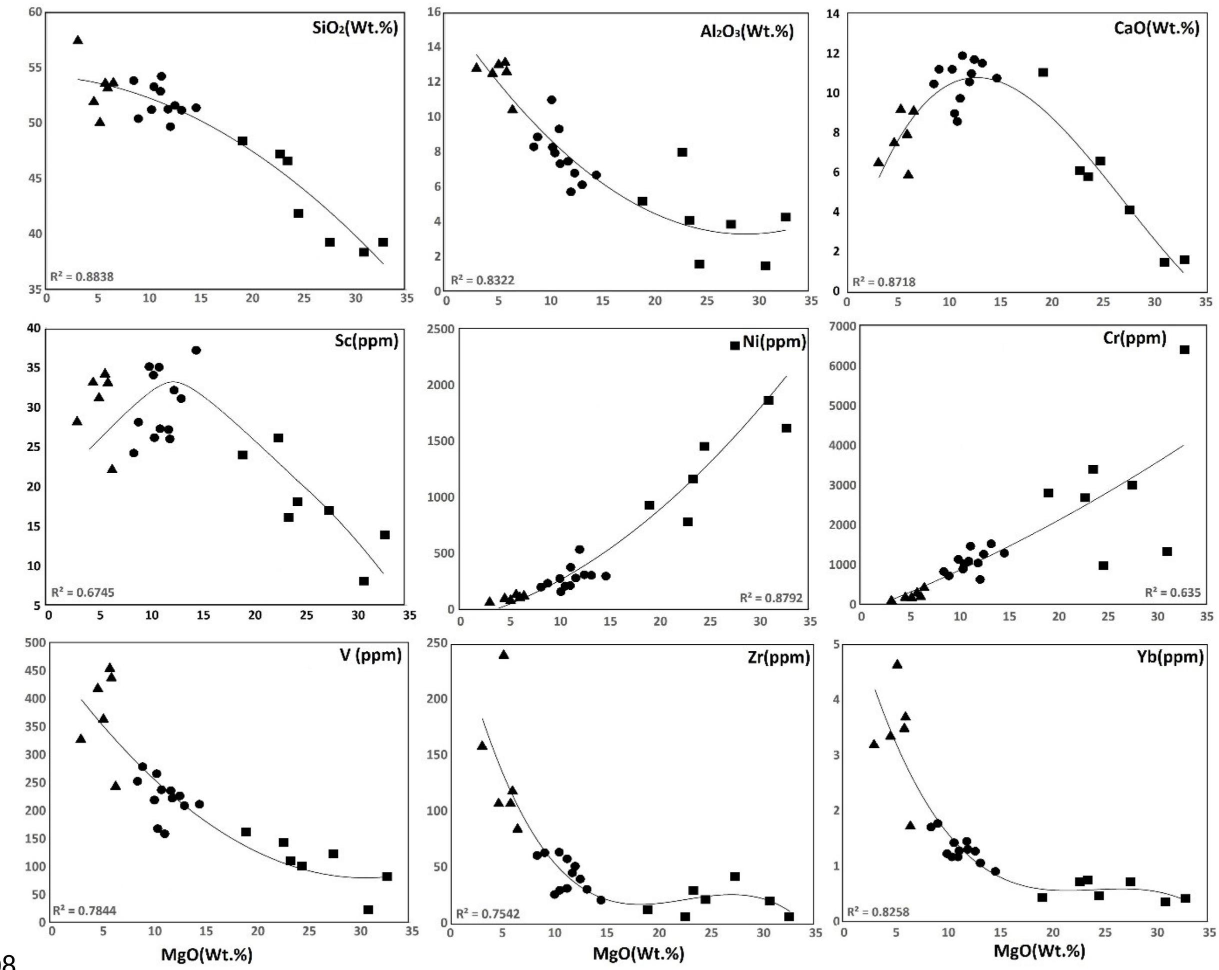

Fig. 6. Bi-variant plots (MgO vs. SiO_2, Al_2O_3, CaO, Sc, Ni, Cr, V, Zr and Yb) of the BGB metavolcanic rocks are showing continuous data array indicated by the projection of best fit polynomial trends. The rock type symbols are same as in Fig. 5C.

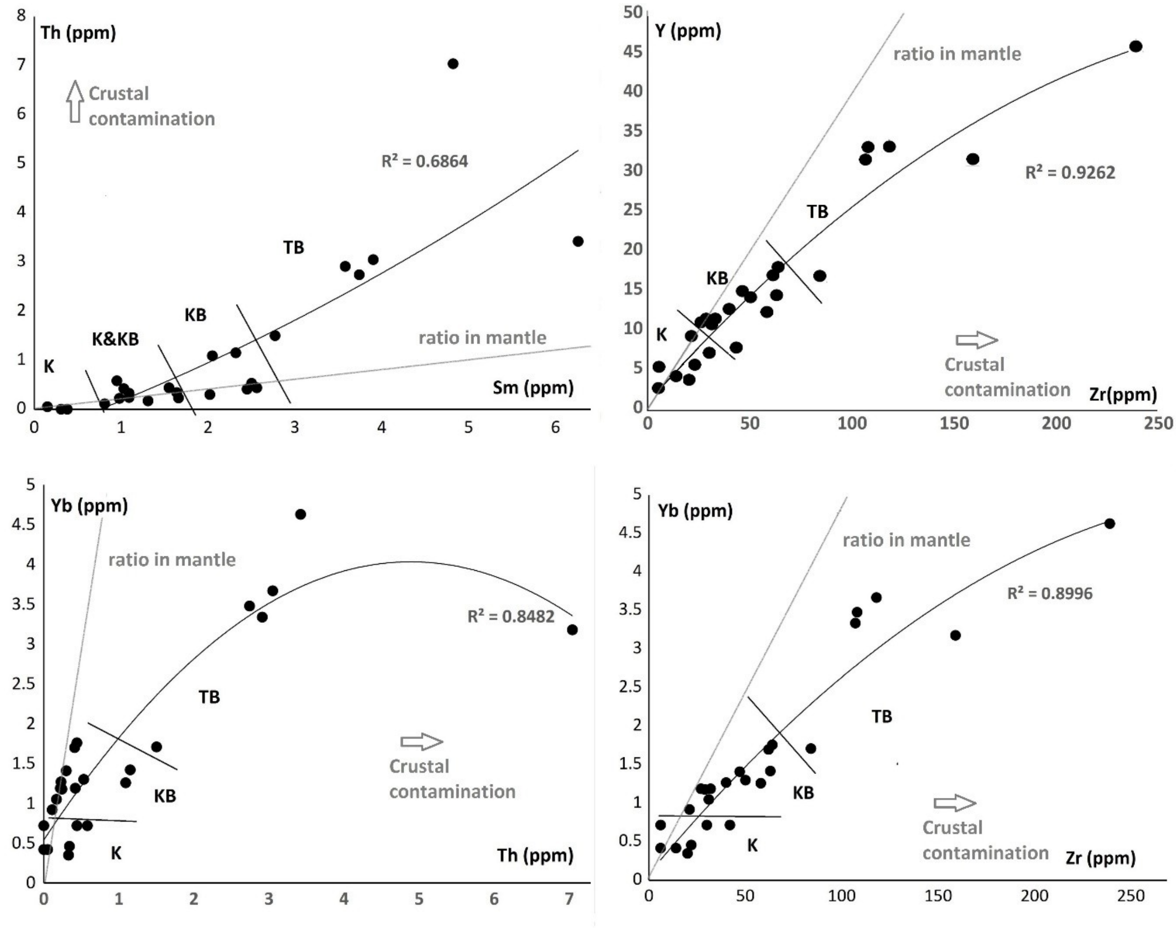

Fig. 7. Bi-variant plots (Zr vs. Nb and Sm, Sm vs. Nb and Th vs. Nb) of the BGB metavolcanic rocks show continuous data array indicated by the projection of best fit polynomial trends. Grey lines mark the elemental ratios in Earth's mantle (Plame and O'Neill, 2014). K~ komatiites, KB~komatiitic basalts, TB~tholeiitic basalts.

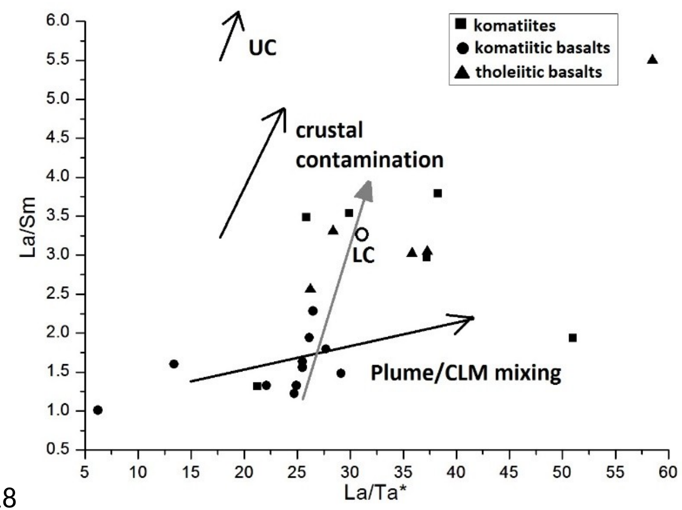

Fig.8. Bi-variant plot (La/Sm vs. La/Ta*, after Lassiter and DePaolo, 1997) of the BGB komatiites and basalts to discriminate processes of mixing with continental lithospheric mantle (CLM) and direct contamination with continental crust. Grey arrow shows the overall trend of komatiites and basalts. Ta*=Nb/17 (Nb/Ta=17, based on a primitive mantle value by Sun and McDonough, 1989). UC~ upper continental crust, LC~ lower continental crust.

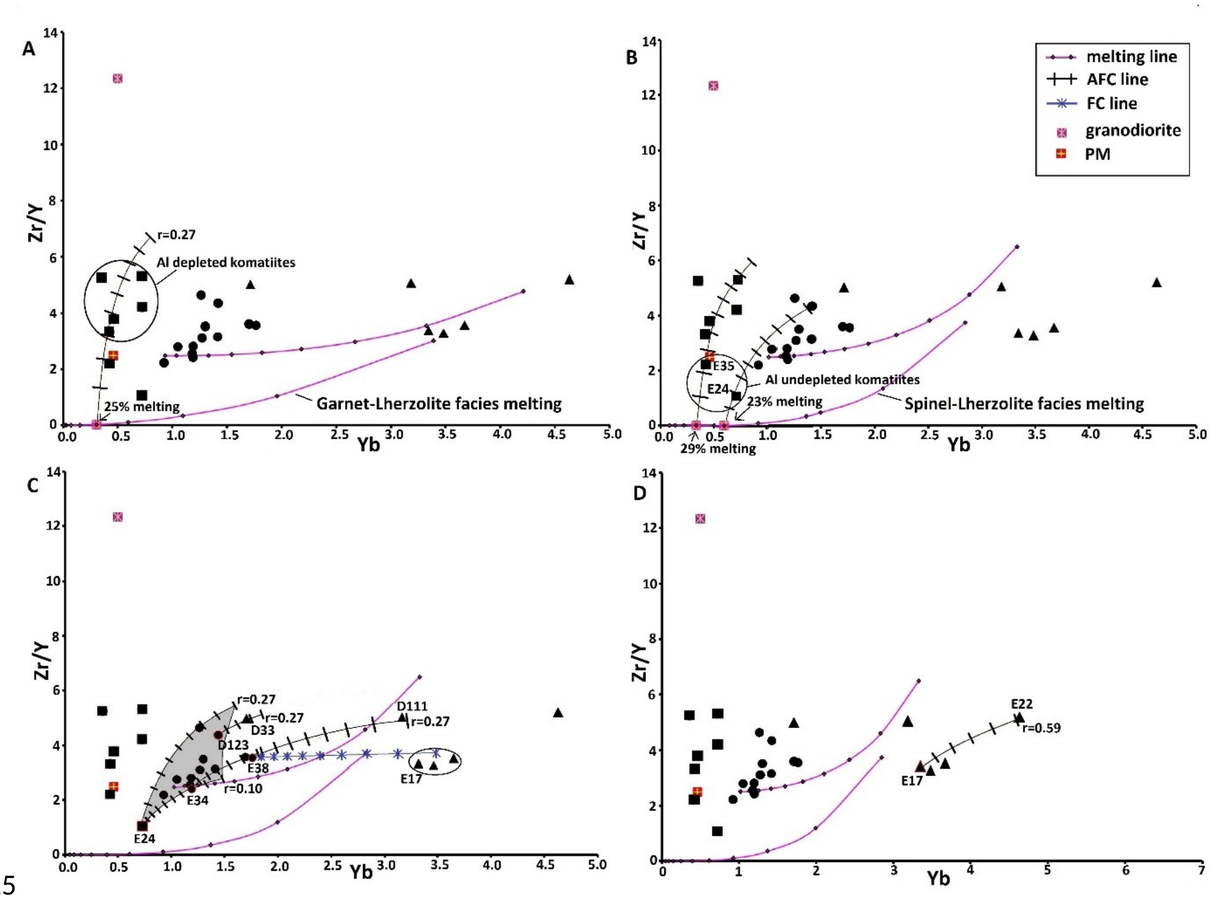

Fig. 9. Melting, assimilation and fractional crystallization modelling of the BGB komatiites and basalts. The rock type symbols are same as in Fig. 8.

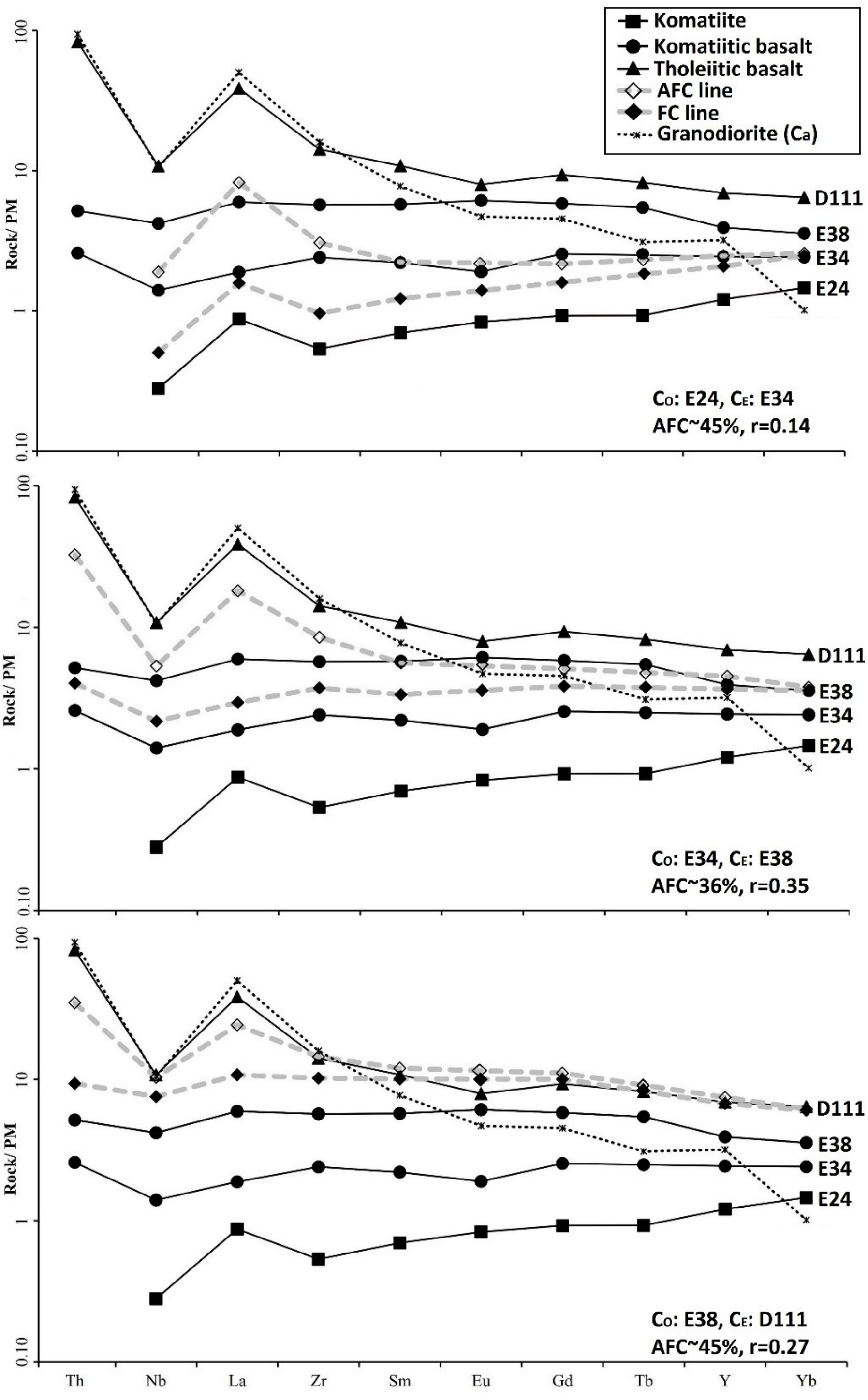

Fig. 10. Assimilation and fractional crystallization (AFC) modelling of selected BGB metavolcanic rocks. C_O~ initial melt composition, C_E~ evolved melt composition, Ca~ composition of the contaminant, PM~ Primitive Mantle (Palme and O'Neill, 2014).

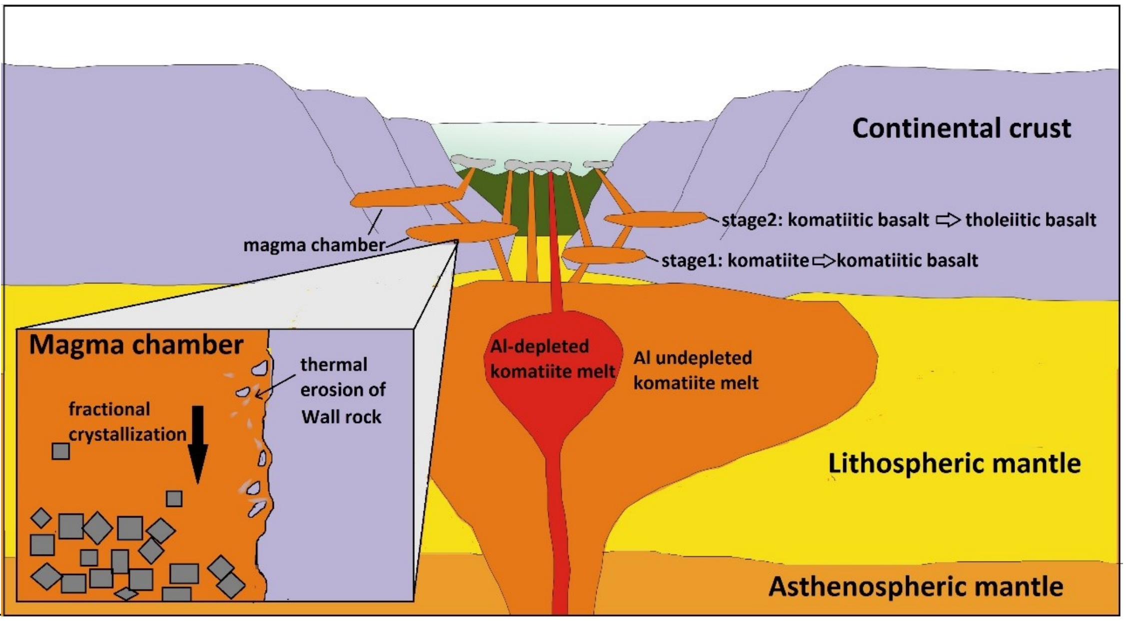

Fig. 11. Simplified sketch geological model of the formation processes for different volcanic rocks in the Badampahar greenstone belt, Singhbhum Craton, Eastern India.

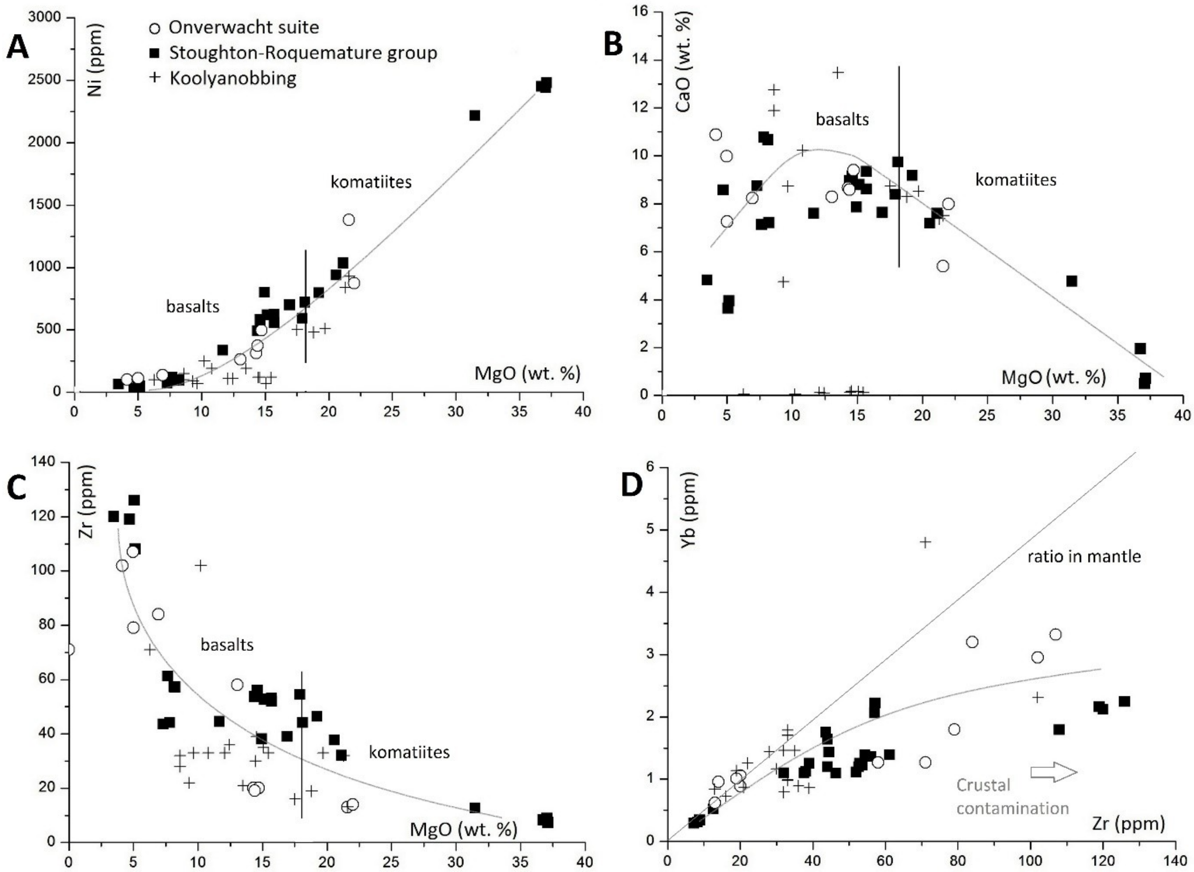

Fig. 12. Bi-variant plots (MgO vs. Ni, CaO and Zr, and Zr vs. Yb) of the komatiites and basalts present in Stoughton-Rouematurе group (~2.7 Ga), Abitibi Greenstone belt, Canada (Dostal and Mueller, 2013), Koolyanobbing greenstone belt (~3.0 Ga), Yilgarn Craton, Australia (Angerer et al., 2013), and Hooggenoeg Complex, Onverwacht suite (~3.5-3.3 Ga), Barberton greenstone belt, South Africa (Furnes et al., 2012). The plots show continuous data array of the komatiites and basalts indicated by the projection of best fit polynomial trends. Grey straight line in Fig. 11D marks the elemental ratios in Earth’s mantle (Plame and O’Neill, 2014).